Nanoparticle-based combination drug delivery systems for effective cancer treatment

He, Y.

Chapter 5

Effective breast cancer therapy based on palmitic acid-loaded plga nanoparticles

This chapter was adapted from “He, Y.; de Araújo Júnior, R.F.; Cavalcante, R.S.; Yu, Z.; Schomann, T.; Gu, Z.; Eich, C.; Cruz, L.J. Biomaterials Advances 2023, 145”.

Abstract

While recent advancements in breast cancer treatment have shown promise, systemic application of most drugs often leads to significant side effects. Doxorubicin (DOX), currently a frontline chemotherapeutic agent for breast cancer, lacks specificity for tumor cells and frequently results in drug resistance. Recent studies have highlighted the potential of certain fatty acids (FAs) in inhibiting tumorigenesis. Palmitic acid (PA), a saturated FA, has demonstrated anti-tumor effects across various cancer types and can repolarize M2 macrophages towards the anti-tumorigenic M1 phenotype. However, PA's limited solubility and cellular permeability pose challenges for *in vivo* applications. To overcome these limitations, here, we encapsulated PA into a poly (D,L-lactic co-glycolic acid) (PLGA) nanoparticle (NP) platform, alone and in combination with DOX, to explore PA's potential as mono or combinational breast cancer therapy. Our results showed that PLGA-PA-DOX NPs and PLGA-PA NPs significantly reduced the viability and migratory capacity of breast cancer cells *in vitro*. *In vivo* studies using a murine model of mammary tumors demonstrated that PLGA-PA-NPs were as effective in reducing primary tumor growth and metastasis as NPs loaded with DOX, PA and DOX, or free DOX. At the molecular level, PLGA-PA NPs reduced the expression of genes associated with multi-drug resistance and inhibition of apoptosis, and induced apoptosis via a caspase-3-independent pathway in breast cancer cells. In addition, immunohistochemical analysis of residual tumors showed a reduction in M2 macrophage content and infiltration of leukocytes after treatment of PLGA-PA NPs and PLGA-PA-DOX NPs, suggesting immunomodulatory properties of PA in the tumor microenvironment. In conclusion, the use of PA alone or in combination with DOX may represent a promising novel strategy for the treatment of breast cancer.

1 Introduction

The threat to women's health posed by malignant breast cancer cannot be overstated. Due to different molecular subtypes, risk factors, clinical behaviors, and treatment responses, its heterogeneous nature represents a major obstacle to therapeutical success. Although chemotherapy and radiotherapy can improve the overall survival rate of breast cancer patients, these therapies are associated with serious side effects and drug resistance [1]. Therefore, there is an urgent need to design novel treatment strategies to overcome disease progression and prevent relapse. The tumor microenvironment (TME) plays a critical role in tumor occurrence, progression, metastasis and the development of drug resistance [2].

In the TME, tumor-associated macrophages (TAMs) mainly undergo M2-type polarization, causing an immunosuppressive response and promoting tumor growth and metastasis [3]. Numerous studies have shown that M2-type macrophages can be reprogrammed towards the M1-type, which display anti-tumor properties [4-7]. Inhibition of tumor-promoting M2-type macrophages or modulation of the TAM phenotype have shown promising results in the treatment of cancer [3].

Fatty acids (FA) represent essential building blocks of cell membranes and signaling pathways and play a crucial role in the modulation of cellular activities, such as energy storage, cell differentiation and apoptosis [8,9]. In contrast to healthy cells, cancer cells display an altered lipid metabolism [10]. Indeed, a range of malignant processes, including cell proliferation, migration and development of drug resistance, are linked to increased biosynthesis, oxidation and accumulation of FAs [11]. Both endogenous lipogenesis and extracellular lipids play a role in breast cancer development and progression [12], and several genes involved in lipid biosynthesis and adipocyte formation are simultaneously upregulated in breast tumors [13]. Increased FA synthase expression has been reported in HER2+ breast cancer [14]. Moreover, the mammary glands are rich in adipocytes, which can pass on stored lipids to breast cancer cells [11,15]. Next to breast cancer cells, also TAMs display upregulated lipid biosynthesis pathways, leading to an increased cellular lipid content, which contributes to their pro-tumoral functions [16].

Modulation of the lipid landscape by targeting the lipid metabolism of the breast cancer TME or by application of exogenous FAs has proven effective in overcoming drug resistance and metastasis [17]. Several FAs were reported to alter the viability and function of cancer cells and to regulate TAM generation, polarization and function in the TME. For example, C6-ceramide has been shown to improve the efficacy of immunotherapy in hepatocellular carcinoma by reducing the number of

TAMs and increasing the anti-tumor immune response [18]. Thus, modulating the lipid landscape in the TME could be an effective anti-tumor therapy.

Palmitic acid (PA), a saturated FA found in animal and vegetable oils, has been shown to display anti-tumor activity in a variety of tumor types, including colorectal, liver, prostate and breast cancer [19-24]. In a study by Zhu *et al*., PA was shown to have tumoricidal effects by inhibiting the PI3K/Akt pathway causing cell cycle arrest and inhibition of cancer cell migration and invasion [24]. We and others have recently reported a potent role for exogenously applied PA in decreasing 4T1 breast cancer tumorigenicity by inhibiting cell viability, migration and proliferation [20,25]. In addition, PA has been shown to display immunomodulatory properties. For example, PA was described as activator of toll-like receptor (TLR) 4 and caused an inflammatory responses in obese patients [26]. Di-palmitic acid-conjugated to a TLR agonist could effectively deplete M2 TAMs and induced an anti-tumor immune response in a model of cervical cancer [27]. Similarly, Tsai *et al*. demonstrated that PA induced a pro-inflammatory response in mouse macrophages [28]. Next to tumoricidal effects, we demonstrated that PA could promote the conversion of M2-type into the M1-type macrophages [19,20]. Thus, PA combines multiple advantageous properties that could be exploited for cancer therapy. However, the poor water solubility and cellular impermeability of PA severely limit its use in clinical practice.

Herein, we report a treatment strategy based on PA to elicit breast cancer cell apoptosis and anti-tumor immunity. To overcome the limitations of PA for *in vivo* use, we developed a polymeric PLGA-nanoparticle (NP) platform incorporating PA for mono therapy or in combination with the chemotherapeutic agent doxorubicin (DOX). While DOX easily traverses biological membranes, it displays multiple disadvantages, such as its poor tumor selectivity, susceptibility to drug resistance and serious side effects when administered systemically, including cardiotoxicity, nephrotoxicity, and neurotoxicity [29,30]. When encapsulated into the core of NPs, less severe side effects were reported, compared to systemically applied free DOX [30]. In addition, drug delivery via NPs can effectively improve drug stability, protect the drug from premature degradation and facilitate the cellular drug uptake [29,30]. Poly (lactic acid-glycolic acid copolymer) (PLGA) has been widely used as delivery system for various anticancer drugs because of its good biocompatibility, non-toxicity, biodegradability and sustained release profile [29,31].

Here, we systematically characterized the physicochemical properties of PLGA-PA, PLGA-DOX and PLGA-PA-DOX NPs, including size distribution, surface charge, as well as drug release kinetics. The therapeutic effect of the NPs was assessed *in*

vitro and *in vivo* in the murine triple-negative breast cancer model 4T1. In addition, we analyzed the effect of the different NP formulations on M2 TAMs *in vitro* and in situ in the TME of murine breast tumors. To our knowledge, this is the first therapeutic approach combining PA and DOX in a PLGA-NP platform. Together, our results showed an effective reduction in breast tumor growth and metastasis upon treatment with PLGA-PA-DOX and PLGA-PA NPs. Further analysis revealed the concurrent reduction of M2 TAMs in the breast cancer TME and an increase in infiltrating lymphocytes upon treatment with PLGA-PA NPs (Graphical abstract).

2 Materials and Methods

2.1 Materials and reagents

PLGA polymer (D, L-lactide/glycolide molar ratio of 50:50, M = 17,000 g/mol) was purchased from Carbion PURAC (Amsterdam, the Netherlands). Polyvinyl alcohol (PVA) (M = 13,000−23,000 g/mol, 87−89% hydrolyzed) and chloroform (CHCL3, M = 119.38 g/mol) were provided by Sigma-Aldrich (Merck, Darmstadt, Germany). SV Total RNA Isolation System and CellTiter 96 (R) AQueous MTS Reagent Powder were obtained from Promega (Madison, WI, USA). SnakeSkin™ Dialysis Tubing (3.5 kDa MWCO, 22 mm), High-Capacity RNA-to-cDNA™ Kit, KaryoMAX™Giemsa Staining Solution, PowerUp™ SYBR™ Green Master Mix, LysoTracker™ Deep Red, Dulbecco's Modified Eagle's Medium (DMEM), trypsin, penicillin-streptomycin (10,000 U/mL), TRIzol, anti-caspase-3 (clone 74T2), DAPI (4',6-Diamidino-2-Phenylindole, Dilactate), Alexa Fluor™ 488 Phalloidin and fetal bovine serum (FBS) were obtained from Thermo Scientific™ (Waltham, MA, USA). PA (molecular weight = 256.42 g/mol) was provided by Sigma-Aldrich (Darmstadt, Germany). Anti-mouse CD163-PerCP-eFluor™ 710 (Clone TNKUPJ), anti-mouse CD68-FITC (clone FA-11), and anti-mouse CD86-FITC (clone GL1) were provided by eBioscience (San Diego, CA, USA). PA lissamine rhodamine ([16-N- (lissamine rhodamine ß sulfonyl)amino] palmitic acid) was obtained from Avanti (Alabama, USA). Diaminobenzidine and hematoxylin were purchased from DAKO (Santa Clara, CA, USA). 1,1'-Dioctadecyl-3,3,3',3'-tetramethyl indo dicarbocyanine (DiD), dimethyl sulfoxide (DMSO) and anti-CXCL-12 (clone 79018) were acquired from Invitrogen (Thermo Scientific™, Waltham, Massachusetts, USA). Anti-MMP-2 (clone B84) and anti-NF-κB (clone F-6) was provided by Santa Cruz Biotechnology (Dallas, TX, USA). Biotinylated pan-specific universal secondary antibody and streptavidin/ HRP conjugated antibody were purchased from Vector Labs (Vicbio Biotechnology

Co., Ltd, Beijing, China). Recombinant mouse IL-4, lipopolysaccharide (LPS), and Interferon gamma (IFN-γ) were provided by PeproTech (Rocky Hill, NJ, USA). Doxorubicin hydrochloride (DOX, molecular weight:579.98 g/mol, 98.0−102.0% (HPLC)) was provided by Euroasia Co., Ltd. (Delhi, India).

2.2 Preparation of PLGA NPs

DOX and/or PA-loaded PLGA NPs were synthesized using a double emulsion solvent evaporation method, as described in the literature [32,33]. Briefly, 10 mg DOX was dissolved in 1 mL ultrapure deionized water. Secondly, 150 µL DiD vibrant dye solution (0.5 mg/mL in chloroform), 25 mg PA, and 50 mg PLGA were dissolved in 3 mL chloroform, and then magnetically stirred for 3 min at room temperature (RT). Next, the aqueous solution of DOX was added dropwise to 3 mL of chloroform containing PLGA and PA. Next, a sonicator (250 watts; Sonifier 250; Branson Ultrasonics, Danbury, CT, USA) was used to emulsify the solution for 75 sec to obtain a water-in-oil (W_1/O) primary emulsion. Subsequently, the primary emulsion was emulsified into 20 mL of 5% polyvinyl alcohol (PVA,w/v) in an ice bath using a sonicator to obtain a double emulsion which is water-in-oil-in-water (W_1/O/W_2). Next, the double emulsion was transferred to 15 mL of 2% aqueous PVA (w/v) and stirred on a magnetic stirrer for 4 h to evaporate the chloroform evaporated completely. Then, the NPs were collected by ultracentrifugation (14,000 ×g for 35 min) and subsequently washed 3 times with ultra-pure deionized water to remove free drugs. Finally, the NPs were freeze-dried for 4 days and stored in a −20°C refrigerator until further use.

2.3 Characterization of NPs

The size and zeta potential (surface charge) of the different NP formulations were assessed by means of the dynamic light scattering (DLS) method. In short, 1 mg of NP powder was dissolved in 1 mL of ultrapure water, from which 10 µL of this solution was transferred to 990 µL of water and mixed thoroughly. The 1 mL mixed solution was transferred to a cuvette containing 1 mL of water, followed by a measurement with the Zetasizer (NANO-ZS, Malvern Ltd., UK).

2.4 Particle surface and morphology

The shape and surface morphology of the NPs were visualized and analyzed

by JEOL 2010F transmission electron microscopy (TEM, NFFA, Trieste, ITALY). In short, 1 mg of freeze-dried NPs was dissolved in 1 mL of ultrapure water and sonicated in a sonicator for 2 min to mix it well. Then, 20 µL of the NP solution was added onto a Formvar-coated copper grid. Subsequently, 2.3% uranyl acetate was used to negatively stain the NPs for 1 min. The grid was air-dried and the sample was analyzed by transmission electron microscopy (Tecnai 12 Biotwin) (FEI, the Netherlands) at a voltage of 120 kV.

As mentioned elsewhere [30,34], the encapsulation efficacy of DOX into PLGA NPs was assessed by a SpectraMax® iD3 Multi-Mode Microplate Readers (Molecular Devices, Silicon Valley, CA, USA). Briefly, 1 mg of freeze-dried DOX-loaded NPs were dissolved in 0.4 mL of DMSO. Acetic acid was added to compensate for the basicity of this solvent. Aliquots of the dissolved PLGA NPs were transferred to a 96-well plate in 100 µL/wells. Then, the absorbance of the drug was evaluated at 480 nm absorption wavelength by a SpectraMax® iD3 Multi-Mode Microplate Reader. Similarly, the encapsulation efficacy of PA was determined indirectly by encapsulating fluorescence-labeled PA-rhodamine. The absorbance of the PA-rhodamine was evaluated at 580 nm absorption wavelength by a Microplate Reader. This experiment used a calibration curve obtained from a dilution (0−500 µg/mL) of PA-rhodamine and DOX (0−1 mg/mL) to calculate the concentration of PA and DOX from the measured fluorescence intensity values. The percentage of DOX and/or PA-rhodamine loading and encapsulation efficiency in NPs was calculated by the following formula:

$$\text{Encapsulation rate (\%)} = \frac{\text{amount of drug released from lyophilized PLGA NPs}}{\text{amount of drug originally used to prepare NPs}} \times 100\%$$

$$\text{Drug loading (\%)} = \frac{\text{amount of drug found in lyophilized NPs}}{\text{amount of lyophilized NPs}} \times 100\%$$

2.6 UPLC-MS/MS

In addition, the encapsulation efficacy of PA inside the PLGA NPs was determined by ultraperformance liquid chromatography-tandem mass spectrometry (UPLS-MS, Milford, MA, USA). Briefly, a sample of 0.5 mg/mL PA was prepared, and after the sample had dissolved sufficiently, 40 µL sample was dispersed into 500 µL of methanol and treated in an ultrasonicator for 10 min, centrifuged (3,000 ×g for 15

min) and aliquoted. Next, the solution of PA standards was prepared in methanol and used as a calibration curve to prepare 8 concentration levels ranging from 3.125 to 400 μg/mL. The mobile phase included acetonitrile/water (60:40, v/v; solvent A) and isopropanol/acetonitrile solution of ammonium acetate (90:10, v/v; solvent B). 0.4 mL per min was set as the flow rate, the injector temperature was 4°C, the injection volume was set at 5 μL, the spray voltage was 4 kV, and six consecutive assays were performed for each sample to stabilize the repeatability of the instrument.

2.7 *In vitro* drug release studies

To determine the *in vitro* drug release, 2 mg of PLGA NPs encapsulating DOX and/or PA-rhodamine were dissolved in pH 7.4, pH 6.5, and pH 5.0 PBS and placed in a dialysis tube (3.5 kDa MWCO). Then the dialysis tube was placed in a tube containing 25 mL of PBS. The dialysis tube filled with NPs was continuously stirred in a shaker incubator at 150 rpm and 36.5°C. The content of DOX and PA in the PBS was measured at 480 nm and 580nm by a SpectraMax M3 Multi-Mode Microplate Reader (Molecular Devices, Silicon Valley, CA, USA) photo spectrometer at predetermined time intervals. Each drug release experiment was performed in triplicate and repeated three times.

2.8 Stability of NPs

A NP stability study was conducted for 7 days, as previously described [35]. In short, 2 mg of PLGA-DOX NPs and PLGA-PA-DOX NPs were dissolved in 10 mL of DMEM containing 50% FCS or 10% FCS and kept in a shaker at 100 rpm and 36.5°C. A 1 mL sample was removed from the NP solution each day for 7 days and the size and zeta potential of the samples were evaluated by DLS.

2.9 Cell culture

The 4T1 (ATCC No. CRL-2539™) and RAW 264.7 (ATCC No. TIB-71™) cell lines were obtained from ATCC, and they were cultured in DMEM containing 1% penicillin-streptomycin (p/s) and 10% FBS. Both of these cell lines were maintained in a 37°C incubator with 95% relative humidity (RH) and 5% CO_2. The cells were passaged (at a ratio of 1:10) when the cells reached a density of about 80–90%.

2.10 *In vitro* cytotoxicity test

The anti-tumor activity of the NPs on 4T1 breast cancer cells was assessed by MTS assay. This colorimetric method assesses the viability of cells by measuring the ability of dehydrogenase present in live cells to produce formazan at 490 nm. 4T1 cells (1×10^4 cells/well) were seeded in a 96-well plate and cultured in a 37°C and 5% CO_2 incubator for 24 h. Afterward, the old medium was replaced with a medium supplemented with NPs or free DOX. After 48 h, the cells were treated with MTS reagent, incubated at a 37°C incubator for 1.5 h, and the absorbance was evaluated by absorption spectrophotometry at 490 nm absorption wavelength with a SpectraMax M3 Multi-Mode Microplate Reader.

2.11 Cell apoptosis assay

In order to detect whether NPs can cause apoptosis or necrosis of breast cancer cells, we used Annexin-V-FITC and 7AAD staining. In short, 4T1 cells (1×10^5 cells/well) were seeded in a 24-well plate. When the growth density of the cells reached 80–95%, the cells were treated with 25 μg/mL of different NP formulations. After 48 h of incubation, the cells were detached with trypsin. According to the protocol's instructions, the 4T1 cells were stained with Annexin-V-FITC (to identify apoptotic cells) and 7AAD (to stain necrotic cells), and analyzed by a BD FACS II flow cytometer (BD Biosciences, NJ, USA).

2.12 Analysis of the cellular NP uptake by immunofluorescence microscopy

Immunofluorescence microscopy was used to visualize the cellular uptake of NPs after 1, 4, 24, and 48 h of incubation. In short, 4T1 cells were seeded onto a cover glass in a 24-well plate (3×10^4 cells/well) and incubated in with 80 μg/mL NPs in serum-free (SF) medium at 37°C and 5% CO_2 incubator for the indicated time points. After incubation, 4T1 cells were fixed with 1% paraformaldehyde (PFA) for 20 min. Subsequently, 4T1 cells were washed 2 times in PBS, followed by permeabilization with 0.1% Triton-X-100 (Sigma-Aldrich, Merck, Darmstadt, Germany) in PBS at RT for 10 min and two washing steps in PBS. Actin was stained with phalloidin-FITC (green) at 37°C for 40 min, and the nucleus was stained with DAPI (blue) at RT for 15 min. Fluorescence images were obtained with the immunofluorescence microscope imaging system (Leica AF6000, Leica Microsystems CMS GmbH, Mannheim, Germany).

2.13 Analysis of the cellular NP uptake of by flow cytometry

The internalization of NPs in 4T1 cells was analyzed by flow cytometry. To this end, 4T1 cells (7×10^4 cells per well) in a 24-well plate were cultured in the presence of PLGA-PA NPs, PLGA-DOX NPs, PLGA NPs or PLGA-PA-DOX NPs at 37°C for 1, 4, 8, 12, 24, and 48 h. After incubation, the cells were detached with trypsin. Subsequently, the cells were centrifuged, washed once in PBS, and resuspended in FACS buffer (PBS, 0.1% NaN_3,1% BSA). The cellular uptake of the different NP formulations was evaluated by flow cytometry. The data was analyzed using FlowJo™ v10.7.1 software (BD Biosciences).

2.14 Analysis of the intracellular NP localization by confocal microscopy

4T1 cells (4×10^4 cells per well) were seeded on sterile cover glasses. After 24 h, the cells were treated with 80 µg/mL NPs for 1, 4, 24 and 48 h, followed by three washing steps in PBS. Subsequently, 4T1 cells were fixed with 4% PFA at RT for 15 min. After fixation, the cells were washed 3 times with PBS, and permeabilized with 0.1% Triton-X 100 /PBS at RT for 10 min. Finally, the actin cytoskeleton was stained with phalloidin and the nuclei with DAPI. After several washing steps in PBS, the cover glasses were sealed in mounting medium and the samples were analyzed with a Confocal Laser Scanning Microscope (CLSM, Leica TCS SP8). The Leica Application Suite X software were used to analyze the images.

When lysosomes were additionally stained with LysoTracker™ Deep Red (excitation/emission of 647/668 nm) to analyze the colocalization of NPs/PA with lysosomes, the following protocol was used: 4T1 cells (5×10^3 cells per well) were seeded in a 24-well plate containing a cover glass (Φ 13 mm, VWR International B.V., Amsterdam, the Netherlands). After incubation at 37°C for 24 h, the culture medium was removed and 4T1 cells were treated with culture medium containing 80 µg/mL PLGA-PA NPs and incubated for 1, 4, 8, 24 and 48 h. After incubation, cells were washed 5 times and then LysoTracker™ Deep Red diluted in culture medium was added and cells were incubated at 37°C for 50 min. Subsequently, the cells were fixed with 4% PFA at RT for 15 min. Actin skeleton and nuclei were further stained as described above.

2.15 Polarization of RAW 264.7 cells towards M2 macrophages

The effect of PA-containing NPs on M2 macrophages was examined by flow

cytometry. Briefly, RAW 264.7 cells were seeded into 24-well plates at a concentration of 8 × 10^4 cells/well and incubated for 24 h. Then, the medium was supplemented with 20 ng/mL IL-4 for 24 h. M2-polarized TAMs were then incubated with SF medium supplemented with IL-4 for 48 h.

To assess the effect of PA-containing NPs on M2-type macrophages, RAW 264.7 cells were cultured in medium supplemented with 20 ng/mL IL-4 for 24 h followed by incubation with SF medium containing 25 μg/mL PLGA-PA NPs and IL-4 for 48 h, as described above.

2.16 Wound healing assay

To explore the effect of NP treatment on the invasive potential of 4T1, we performed a wound healing assay during 48 h of NP incubation. 4T1 cells were seeded (3 × 10^4 cells/150 μL/well) in an incucyte® Clearview 96-well plate (Essen BioScience, Ltd., Newark, UK) and incubated in a 37°C, 5% CO_2 incubator for 24 h. When the cell density reached 95–100% confluence, IncuCyte® Cell Migration Kit was used to create a "wound" in a petri dish and the cells were further cultured with serum-free medium containing 10 μg/mL mitomycin for 1.5 h to inhibit 4T1 cell proliferation. Subsequently, 4T1 cancer cells were treated with serum-free medium containing NPs at a concentration of 5 μg/mL. Wound healing images were collected every 2 h, and the IncuCyte® live-cell analysis system (Essen BioScience, Ltd., Newark, UK) was used to analyze the wound healing rate.

2.17 Animals

All animal procedures were approved by the Laboratory Animal Management Committee and Ethics Committee of Federal University of Rio Grande Norte (No. 063/2016) and strictly followed the updated ARRIVE guidelines [36]. BALB/c mice (female, 7–9 weeks-old, weight 22–26 g) were provided by Keizo Asami Immunopathology Laboratory (LIKA; Recife, PE, Brazil). Mice were kept in an air-conditioned room at 21–22°C, 56% relative humidity, specific pathogen-free conditions, and a 12-h light/dark (LD) cycle. A group of five mice was housed in a cage and mice had free access to food and water. These mice were randomly grouped (n = 6) and kept in different cages. After the mice were adapted to the environment for 1 week, the animal experiment was started.

2.18 Orthotopic tumor model

BALB/c mice were anesthetized with a combination of xylazine and ketamine, and 4T1 cells (1×10^6 cells in 100 μL DMEM without FBS) were injected into the lower part of the fourth left breast of the mouse. The mice were randomly divided into six groups, each group containing 6 mice, and treatment was started when the tumor volume reached 30 mm^3. The following groups were evaluated: untreated group (sterile saline; negative control group), DOX group (5 mg/kg; positive control), PLGA NPs group, PLGA-PA NPs group, PLGA-DOX NPs group and PLGA-PA-DOX NPs group. Mice were injected intratumorally with NPs or 5 mg free DOX. The number of NPs injected in the PLGA-PA-DOX NPs and PLGA-DOX NPs groups were adjusted to match the DOX content in the free DOX group. The number of NPs injected in the PLGA NPs and PLGA-PA NPs groups were adjusted to the number injected in the PLGA-PA-DOX NP group. The treatment was repeated three times (every 5 days). On day 18, the mice were sacrificed by cervical dislocation. The tumor, blood, liver and lungs were collected for histopathology and biochemical analysis.

2.19 Hematology analysis

Using EDTA-K2 (1 mg/mL) as a blood anticoagulant, 50 μL of fresh blood was collected from tail vein puncture on days 7 and 14 after the first treatment, and the hematology analyzers were used to perform standard techniques. Red blood cells and white blood cells were counted by a blood cell counter. Hemoglobin was quantified by RT-qPCR and hematocrit was measured by a hematology analyzer (UniCel® DxH 800, Beckman Coulter, Inc. CA, USA). The blood samples of all experimental animals (n = 4–6) were evaluated in triplicate.

2.20 Histology and immunohistochemistry

The tumors and organs of BALB/c mice were collected for immunohistochemical examination. In short, the mice were sacrificed on day 18 day after tumor inoculation, and the tumor, liver, and lung of the mice were fixed, paraffin-embedded, and sectioned by autopsy. Sections were incubated with anti-caspase-3, anti-*Mmp2*, anti-*Cxcl12*, and anti-*NF-κB* primary antibodies overnight at 4°C. Biotinylated pan-specific antibody was used as the universal secondary antibody, followed by incubation with streptavidin/HRP conjugated and diaminobenzidine for colorimetric staining. Sections were double-stained with hematoxylin and eosin

(H&E) and imaged using a Nikon E200 LED light microscope (Microscope Central, PA, USA) and digital camera (Moticam, San Antonio, TX, USA). Immunoreactivity was analyzed by assessing the ratio of positively stained cells and the intensity of immunofluorescent staining, as described by Charafe-Jauffret *et al*. [37]. The results were evaluated independently by two non-operators. Three tissue sections were assessed for each antibody.

Histopathological changes in the tumor are assessed according to the Histological Alteration Index (HAI). They are divided into 3 stages. stage I, where there is no impairment of organ function; stage II I, where there is severe impairment of organ function affecting normal function; and stage III, where there is very severe and irreversible impairment of organ function. The HAI value for each group of animals was calculated using the formula HAI = 1 × ΣI + 10 × ΣII + 100 × ΣIII [38,39]. Where I, II and III correspond to the number of changes in each stage, the results are divided into 4 categories. 0−15% = normal tissue or mild necrosis with mildly infiltrated lymphocytes; 15−25% = lymphocytes with mild to moderate tissue necrosis or infiltration; 25−50% = lymphocytes with moderate to severe tissue necrosis or infiltration; 50−100% = lymphocytes with severe tissue necrosis or severe infiltration. All sections were scored and the data in each category (I-III) were displayed as percentages of all analyzed sections within each treatment group.

2.21 RT-qPCR

Gene expression analysis was performed on in situ tumors from BALB/c mice. Total RNA from in situ tumors was extracted using TRIzol™ Reagent and purified using the SV Total RNA Isolation System according to the manufacturer's instructions. The $2^{-\Delta\Delta Ct}$ method was used to analyze the breast tumor-associated gene expression data and *β-actin* was considered as a housekeeping gene. Data are presented in triplicate. The primer sequences were as follows: *β-actin* F: 5'-AGGCCAACCTGTAAAAGATG-3', R: 5'-TGTGGTACGAGAGGCATAC-3'; *Nfκb* F: 5'-CCGTCTGTCTGCTCTCTCT-3', R: 5'-CGTAGGGATCATCGTCTGCC -3'; *Apaf-1* F: 5′-TTCCAGTGGCAAGGACACAG-3′, R: 5′-CCACTCTCCACAGGGACAAC-3′; *Mdr1* F: 5′-TCAGCAACAGCAGTCTGGAG-3′; R: 5′-ACTATGAGCACACCAGCACC-3′; *Birc5* (Survivin) F: 5′-AGAACAAAATTGCAAAGGAGACCA-3′, R: 5′-GGCATGTCACTCAGGTCCAA-3′; *Mmp2* F: 5′-AACGGTCGGGAATACAGCAG-3′, R: 5′-GTAAACAAGGCTTCATGGGGG-3′; *Cxcl12* F: 5′-TCAGCCTGAGCTACAGATGC-3′, R: 5′-CTTTAGCTTCGGGTCAATGC-3′.

2.22 Statistical analysis

Unless otherwise stated, data obtained from all experiments are expressed as the mean ± SD (standard deviation) of 3−5 independent repeated experiments. The data were statistically significant using unpaired, Mann-Whitney U test, two-way analysis of variance (ANOVA), and Student's *t*-test in GraphPad Prism 8.1.1 software (GraphPad Software, San Diego, CA, USA). In all analyses, a *p*-value ≤ 0.05 is considered an indicator of statistical significance and is expressed as: * $p \leq 0.05$, ** $p \leq 0.01$, *** $p \leq 0.001$, **** $p \leq 0.0001$.

3 Results

3.1 Physicochemical characterization of NPs

In this study, we synthesized PLGA NPs encapsulating DOX, PA and the fluorescent probe DiD according to the double emulsion solvent evaporation method (W_1/O/W_2; Fig. 1A). First, we assessed the morphological characteristics of PLGA NPs containing PA, DOX, or the combination of DOX and PA, by TEM. PLGA-DOX NPs and PLGA-PA-DOX NPs were spherical with a smooth surface, similar to blank PLGA NPs (Fig. 1B). The particle size, zeta potential and polydispersity index (PDI) of the NPs were further characterized by DLS. As shown in Table 1, the average particle size of PLGA NPs, PLGA-PA NPs, PLGA-DOX NPs and PLGA-PA-DOX NPs was 160.2 ± 10.9 nm, 157.8 ± 9.5 nm, 140.7 ± 11.5 nm and 144.9 ± 5.8 nm, respectively. The surface charge was negative and the PDI values showed a uniform size distribution for all NP formulations (Table 1, Fig. 1C). Our results show that the physicochemical properties of the PLGA NP formulations were not altered by encapsulating PA, DOX or PA and DOX. To confirm the successful co-encapsulation of all compounds, we prepared PLGA NPs containing DOX, PA-rhodamine and DiD. As all these compounds were fluorescent (DOX: excitation 480 nm, emission 560−620 nm; PA-rhodamine: excitation 560 nm, emission 570 nm; and DiD: excitation 633 nm, emission 665 nm), PLGA-PA-rhodamine-DOX NPs were imaged by confocal microscopy to confirm the successful encapsulation of all three compounds into a single PLGA NP (Fig. S1).

Next, we determined the release profile of DOX and PA from PLGA NPs under different pH conditions. To this end, PLGA-PA-DOX NPs were dissolved in PBS (pH 5.0 and 7.4) and incubated under constant agitation at 37°C for 30 days. Under a physiological pH of 7.4, 60% of the encapsulated DOX and 35% of the PA-

rhodamine were rapidly released within the first 48 h (Fig. 1D, F). This was followed by a period of sustained release, which reached a plateau at approximately day 4 and lasted until the end of the analysis. After 30 d, 62% of DOX and 50% of PA were released from the NPs (Fig. 1E, G). Moreover, our results showed that DOX and PA followed different release behaviors from PLGA-PA-DOX NPs at different pH conditions. With a drop in pH from 7.4 to 5.0, the release of DOX significantly increased to 93.6 ± 4.5% (Fig. 1D) within the first 48 h and 100.3 ± 3.9% after 30 d (Fig. 1E). Similar results were obtained for PA. At pH 5.0, 53.1% of PA was released within the first 48 h and 72.78 ± 2.9% after 30 d (Fig. 1F-G). In contrast to DOX, the release of PA was slower and incomplete. In summary, our results showed that PA and DOX were successfully released from PLGA-PA-DOX NPs already within the first 48 h, and that the release of DOX and PA was fastest at low pH.

Next, the stability PLGA-PA-DOX NPs were tested in a medium containing 10% FBS and 50% FBS for 7 days, respectively. DLS and zeta potential measurements did not show significant changes in size and surface charge over 7 days (Fig. 1H-I). These results demonstrate that the NPs were stable in the presence of serum, similar to the physiological condition in the bloodstream.

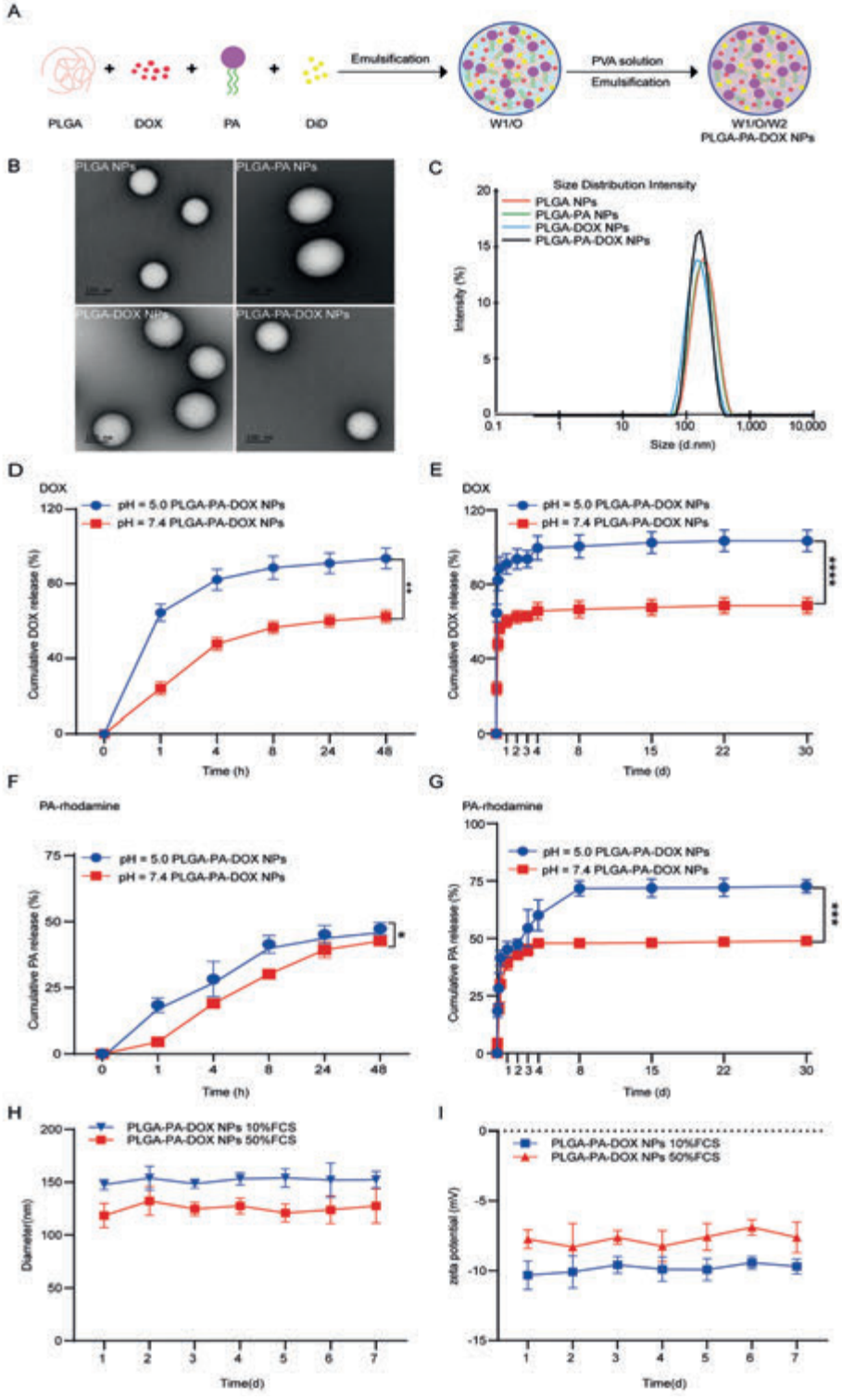
A
PLGA
DOX
PA
DiD
Emulsification
W1/O
PVA solution
Emulsification
W1/O/W2
PLGA-PA-DOX NPs
B
PLGA NPs
PLGA-PA NPs
PLGA-DOX NPs
PLGA-PA-DOX NPs
C
Size Distribution Intensity
PLGA NPs
PLGA-PA NPs
PLGA-DOX NPs
PLGA-PA-DOX NPs
Intensity (%)
Size (d.nm)
D
DOX
pH = 5.0 PLGA-PA-DOX NPs
pH = 7.4 PLGA-PA-DOX NPs
Cumulative DOX release (%)
Time (h)
E
DOX
pH = 5.0 PLGA-PA-DOX NPs
pH = 7.4 PLGA-PA-DOX NPs
Cumulative DOX release (%)
Time (d)
F
PA-rhodamine
pH = 5.0 PLGA-PA-DOX NPs
pH = 7.4 PLGA-PA-DOX NPs
Cumulative PA release (%)
Time (h)
G
PA-rhodamine
pH = 5.0 PLGA-PA-DOX NPs
pH = 7.4 PLGA-PA-DOX NPs
Cumulative PA release (%)
Time (d)
H
PLGA-PA-DOX NPs 10%FCS
PLGA-PA-DOX NPs 50%FCS
Diameter(nm)
Time(d)
I
PLGA-PA-DOX NPs 10%FCS
PLGA-PA-DOX NPs 50%FCS
zeta potential (mV)
Time(d)

Figure 1. Physicochemical properties of PLGA NPs. (A) Schematic illustration of the preparation of PLGA-PA-DOX NPs. (B) TEM images of blank PLGA NPs, PLGA-PA NPs, PLGA-DOX NPs and PLGA-PA-DOX NPs. Scale bar = 100 nm. (C) Representative DLS measurements of the different PLGA NP formulations. Quantification of the cumulative DOX release (%) from PLGA-PA-DOX NPs over (D) 48 h and (E) 30 d, measured in PBS at pH 5.0 and 7.4. Quantification of the cumulative PA release (%) from PLGA-PA-DOX NPs after (F) 48 h and (G) 30 d in PBS at pH 5.0 and 7.4. Stability assessment of PLGA-PA-DOX NPs over 7 d in PBS containing 10% and 50% FBS. Measurement of (H) size and (I) zeta potential. The data is presented as the mean ± SD, n = 3. * $p \leq 0.05$, *** $p \leq 0.001$, **** $p \leq$ 0,0001.

Table 1. Summary of NP particle size, zeta potential, PDI, and drug-loading efficacy of the different PLGA NP formulations

Formulation	Particle size (nm)	Zeta Potential (mV)	PDI	Drug loading (%)-PA	Drug loading (%)-DOX
PLGA NPs	160.2 ± 10.9	-9.7 ± 3.5	0.11 ± 0.03	-	-
PLGA-PA NPs	157.8 ± 9.5	-10.9 ± 2.4	0.12 ± 0.03	48.1 ± 1.5	-
PLGA-DOX NPs	140.7 ± 11.5	-8.9 ± 2.2	0.259 ± 0.08	-	9.5 ± 0.1
PLGA-PA-DOX NPs	144.9 ± 5.8	-10.1 ± 2.6	0.147 ± 0.02	50.9 ± 1.7	11.5 ± 0.2

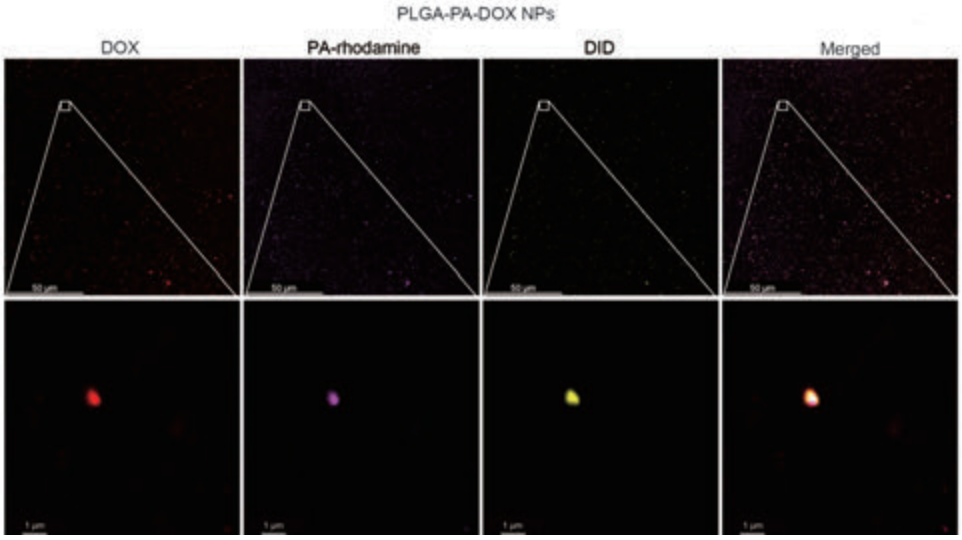

Supplementary Figure 1. PLGA-PA-DOX NPs imaged by CLSM. PLGA-PA-DOX NPs were dissolved in water and then evenly coated onto glass cover slips. DOX,

red; PA-rhodamine, magenta; DiD, yellow. Scale bars upper panel = 50 μm, scale bars lower panel = 1 μm.

3.2 Time-dependent increase of PLGA-PA-DOX NP uptake by 4T1 breast cancer cells

The ability of tumor cells to take up NPs is linked to the efficacy of the nano drugs [40]. Therefore, we assessed the uptake behavior of PLGA-DOX NPs and PLGA-PA-DOX NPs in 4T1 cells by CLSM and flow cytometry. First, flow cytometry was used to quantitatively track the cellular uptake behavior of PLGA-DOX NPs and PLGA-PA-DOX NPs by 4T1 cells at different time points (1, 4, 24, and 48 h; Fig. 2A−B). The uptake of free DOX, PLGA-DOX NPs and PLGA-PA-DOX NPs (containing equal amounts of DOX) by 4T1 cells increased progressively with increasing incubation time. After 1 h and 4 h of incubation, the uptake of free DOX was higher than PLGA-DOX NPs and PLGA-PA-DOX NPs. However, at later time points (24 h and 48 h), there was no significant difference between free DOX and DOX-encapsulating NPs (Fig. 2A−B). These results are consistent with our release kinetics study, showing that approximately 60% of DOX was released within the first 48 h at physiological pH of 7.4. Next, cellular inspection by CLSM allowed visualization of the intracellular routing of free DOX, blank PLGA NPs, PLGA-DOX NPs and PLGA-PA-DOX NPs in 4T1 cells. With increasing incubation time, free DOX rapidly accumulated in the nucleus of 4T1 cells (Fig. 2C), while control (DiD-labeled) PLGA NPs showed a gradual increase in NP accumulation in the cytoplasm (Fig. 2D). When co-encapsulated, analysis of the intracellular distribution of DOX showed that, with increasing incubation time, DOX was released from the DiD-containing NPs and accumulated in the nucleus, while a fraction of non-released DOX remained in the NPs (Fig. 2E). NP uptake, intracellular distribution and release of DOX were not altered when PA was co-encapsulated into the NPs (Fig. 2F).

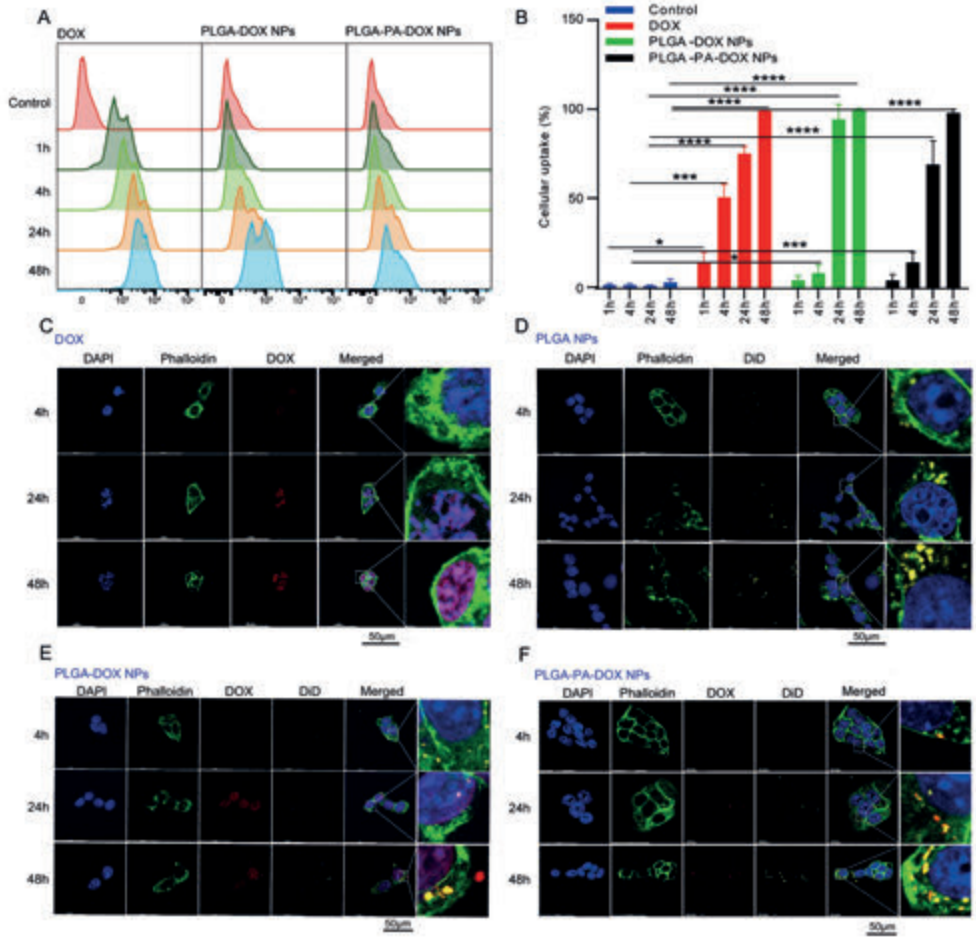

Figure 2. Uptake and intracellular routing of DOX and PLGA NPs. (A) Representative flow cytometric plots of 4T1 cells incubated with free DOX, PLGA-DOX NPs and PLGA-PA-DOX NPs for 1, 4, 24 and 48 h at 37°C. The amount of intracellular DOX was determined by flow cytometry. (B) Quantification of the percentage of DOX-positive 4T1 cells. The intracellular uptake and distribution of (C) DOX, (D) PLGA-DiD NPs, (E) PLGA-DOX-DiD NPs and (F) PLGA-PA-DOX-DiD NPs were further analyzed by CLSM using a 100 × oil immersion objective. The nucleus was labeled with DAPI (blue) and the actin skeleton was labeled with phalloidin (green). DiD, yellow; DOX, red. Scale bar are indicated. All *p*-values were generated using Student's *t*-test. * $p \leq 0.05$, *** $p \leq 0.001$, **** $p \leq 0.0001$.

3.3 PLGA-PA and PLGA-PA-DOX reduce 4T1 cell viability and induce apoptosis

The effect of the different PLGA NP formulations on the viability of 4T1 breast cancer cells were shown in Fig. 3. First, we determined the inhibitory value 50 (IC_{50}) of the free agents by MTS assay. We found that 10.54 µg/mL of free DOX and 66.86 µg/mL of PA resulted in a 50% reduction in metabolic activity of 4T1 (Fig. 3A-B). Next, we assessed the cytotoxic effect of blank (control) PLGA NPs as well as NPs loaded with DOX, PA and DOX and PA together on 4T1 cells (Fig. 3C-F). The IC_{50} of blank PLGA NPs was determined as 20.261 mg/mL, indicating that blank PLGA NPs were only toxic at high concentrations. The inhibitory dose of PLGA-PA NPs was (214 µg/mL; Fig. 3D). As for the drug-loaded NPs, already 7.6 µg/mL of PLGA-DOX NPs and 7.5 µg/mL of PLGA-PA-DOX NPs reduced 4T1 cell viability by 50% (Fig. 3E-F). To directly compare the effect of encapsulated DOX with free DOX, we treated the cells with equal amounts of encapsulated DOX and control NPs (Fig. 3G). At 65.4 µg/mL of PLGA-DOX NPs (equivalent to 7.5 µg/mL free DOX), the viability of 4T1 cells was reduced by 44.4%. At the same NP concentration, PLGA-PA NPs significantly reduced the viability of 4T1 cells by 35.8% (Fig. 3G). When 4T1 cells were treated with an equal concentration of NPs containing both DOX and PA, the metabolic activity was further reduced by 70%, indicating an additive effect of co-delivered PA and DOX. We then quantified the necrosis/apoptosis rate of 4T1 cells after free DOX and PA treatment by Annexin V/7AAD staining and flow cytometry (Fig. 3H). Based on the results of the cell viability assay, we treated 4T1 cells with DOX at concentrations of 2.88 µg/mL and 7.52 µg/mL and PA at 12.75 µg/mL and 32.70 µg/mL, respectively. and quantified early (annexin V+, 7-AAD-) and late apoptosis (annexin V+, 7-AAD+) in 4T1 cells. As shown in Figure 3H, after 24 h incubation, approximately 28.72% and 34.46% of cells in the DOX-treated groups underwent apoptosis; whereas approximately 18.69% and 20.17% of cells in the PA-treated groups underwent apoptosis, respectively. After 48 h incubation, apoptosis rate increased to 35.65% and 58.1% in the DOX-treated group; while the percentage of Annexin V-positive cells increased to 20.39% and 32.98% in the PA-treated groups, respectively.

To determine whether the reduction in metabolic activity in response to different PLGA NP formulations containing DOX and PA was indeed due to a reduction in cellular viability, we quantified the necrosis/apoptosis rate of 4T1 cells after NP treatment by Annexin V/7AAD staining and flow cytometry (Fig. 3I). Early (Annexin V+, 7-AAD-) and late apoptosis (Annexin V+, 7-AAD+) of 4T1 cells were quantified after treatment with 25 µg/mL of PLGA NPs, PLGA-PA NPs, PLGA-DOX NPs and PLGA-PA-DOX NPs for 24 h and 48 h. As shown in Figure 3I, the viability of 4T1

cells was above 90% even after prolonged treatment time with blank PLGA NPs, indicating that PLGA NPs were not significantly cytotoxic to 4T1 cells ($p > 0.05$). In contrast, treatment with PLGA-PA NPs, PLGA-DOX NPs and PLGA-PA-DOX NPs led to an increase in the percentages of Annexin V positive cells after 24 h (17.41%, 35.3% and 27.54%, respectively) and 48 h (19.3%, 42.38% and 53.6%, respectively) (Fig. 3I). After 48 h, an additive effect of PA and DOX on the apoptosis rate could be observed, indicating that co-encapsulated PA and DOX could increase the therapeutic effect. In summary, our results show that PLGA-PA NPs and PLGA-PA-DOX induced apoptosis in 4T1 cells, and co-delivery of DOX and PA by PLGA NPs further reduced the viability of 4T1 breast cancer cells. Furthermore, by comparing the free DOX and PA treated groups with the NPs treated groups, we found that the probability of late apoptosis and necrosis in free DOX and PA induced cells was significantly higher than that in the NPs treated group. This is also side evidence that NPs effectively delayed the toxicity of free DOX and PA to cells.

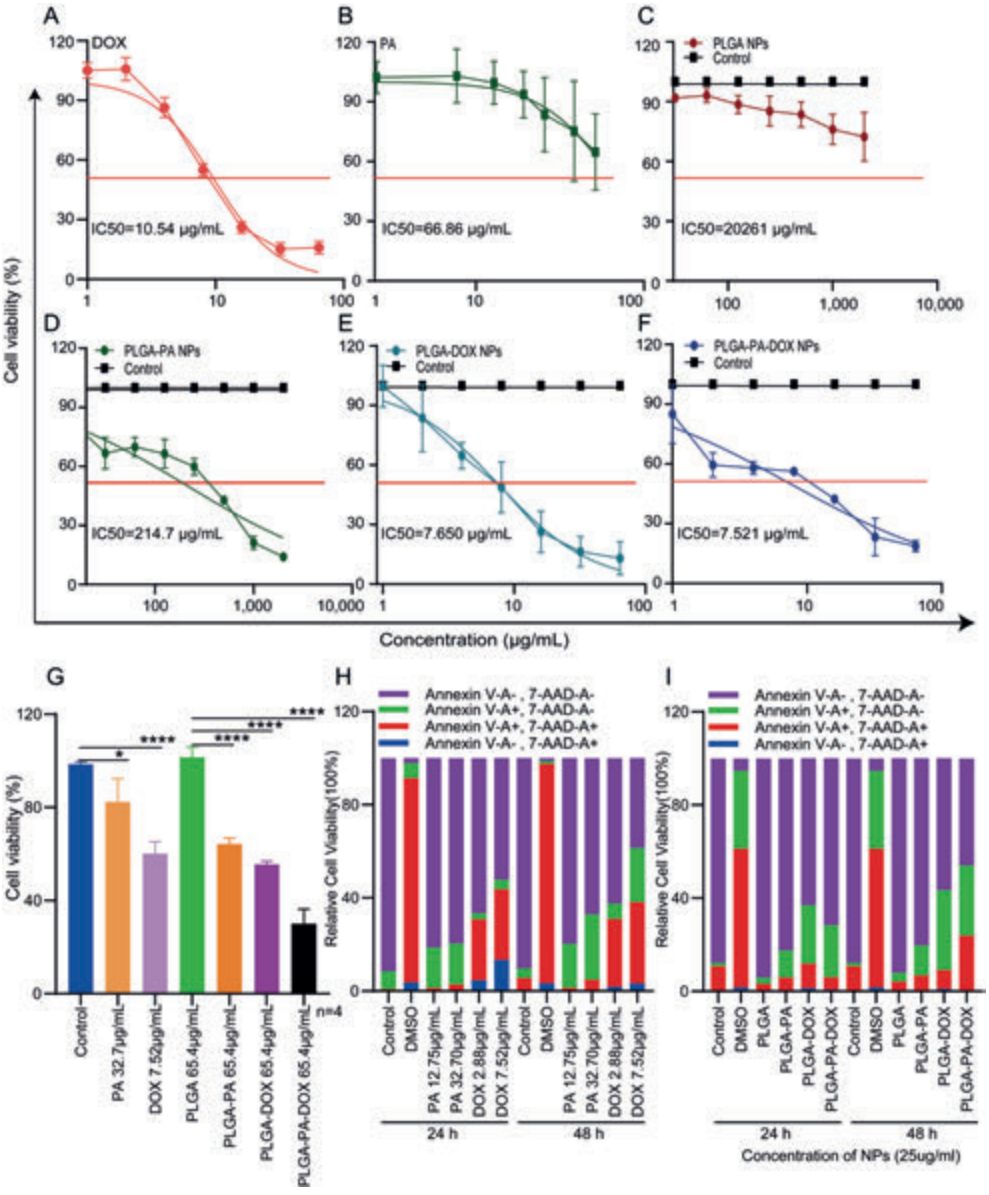

Figure 3. Comparison of the effect of free and encapsulated PA and DOX on the viability of 4T1 cells measured by MTS assay. IC_{50} of (A) free DOX, (B) free PA, and different formulations of PLGA NPs (C-F) on 4T1 cells. (G) To directly compare the effect of encapsulated DOX and PA to free compounds, the concentration of NPs was adjusted to match the concentration of free DOX and PA. 4T1 cells were treated with 65.4 μg/mL of NPs (equivalent to 7.5214 μg/mL free DOX and 32.7 μg/mL free PA) or control NPs. Cell viability was measured by MTS assay. (H-I) Annexin V/7AAD labeling to determine apoptosis rate in 4T1 cells treated with

free DOX and PA and NPs for 24 h and 48 h. Data were analyzed using a one-way ANOVA with post-hoc Bonferroni correction; * $p \leq 0.05$, **** $p \leq 0.0001$. The data represent the mean ± SEM of five independent experiments.

3.4 Intracellular release kinetics and routing of PA

Next, we analyzed the intracellular routing and release of PA from PLGA-PA NPs. To this end, we prepared PLGA NPs, which encapsulated DiD and PA-rhodamine, and incubated 4T1 cells with PLGA-PA-rhodamine NPs for 1, 4, 12, 24 and 48 h. Subsequently, we analyzed the intracellular release of PA-rhodamine by CLSM. In line with the results presented in Figure 3, PLGA-PA NPs accumulated in the cytoplasm over time (Fig. 4A). Quantification of the fluorescence intensity of PA-rhodamine showed that PA-rhodamine could gradually be detected in the cytoplasm as the incubation time increased (Fig. 4B). NPs enter cells via endocytic vesicles, which then fuse with prelysosomes and mature into lysosomes. An important prerequisite for intracellular drug delivery is that NPs efficiently escape the endosomal/lysosomal pathway into the cytoplasm. To explore the intracellular routing of PLGA-PA-rhodamine NPs and colocalization with lysosomes, 4T1 cells were treated with NPs, co-labeled with LysoTracker and analyzed by CLSM (Fig. 4C). To this end, 4T1 cells were incubated with 100 µg PLGA-PA-rhodamine NPs (containing 48.1 µg PA) for 0, 4, 24 and 48 h and subsequently labeled with LysoTracker. In line with the flow cytometry data, 4T1 cells gradually took up NPs over time (Fig. 4A). Visual inspection revealed that, 4 h after NP uptake, PA-rhodamine could be detected inside of 4T1 cells, and a fraction of the rhodamine signal colocalized with lysosomes. At later time points the amount of intracellular PA-rhodamine increased, but the colocalization with lysomes decreased. Quantification of the Mander's overlap coefficient of the PA-rhodamne signal from the NPs and LysoTracker confirmed a signficantly higher colocalization of PA-rhodamine after 4 h, compared to 12, 24 and 48 h (Fig. 4D).

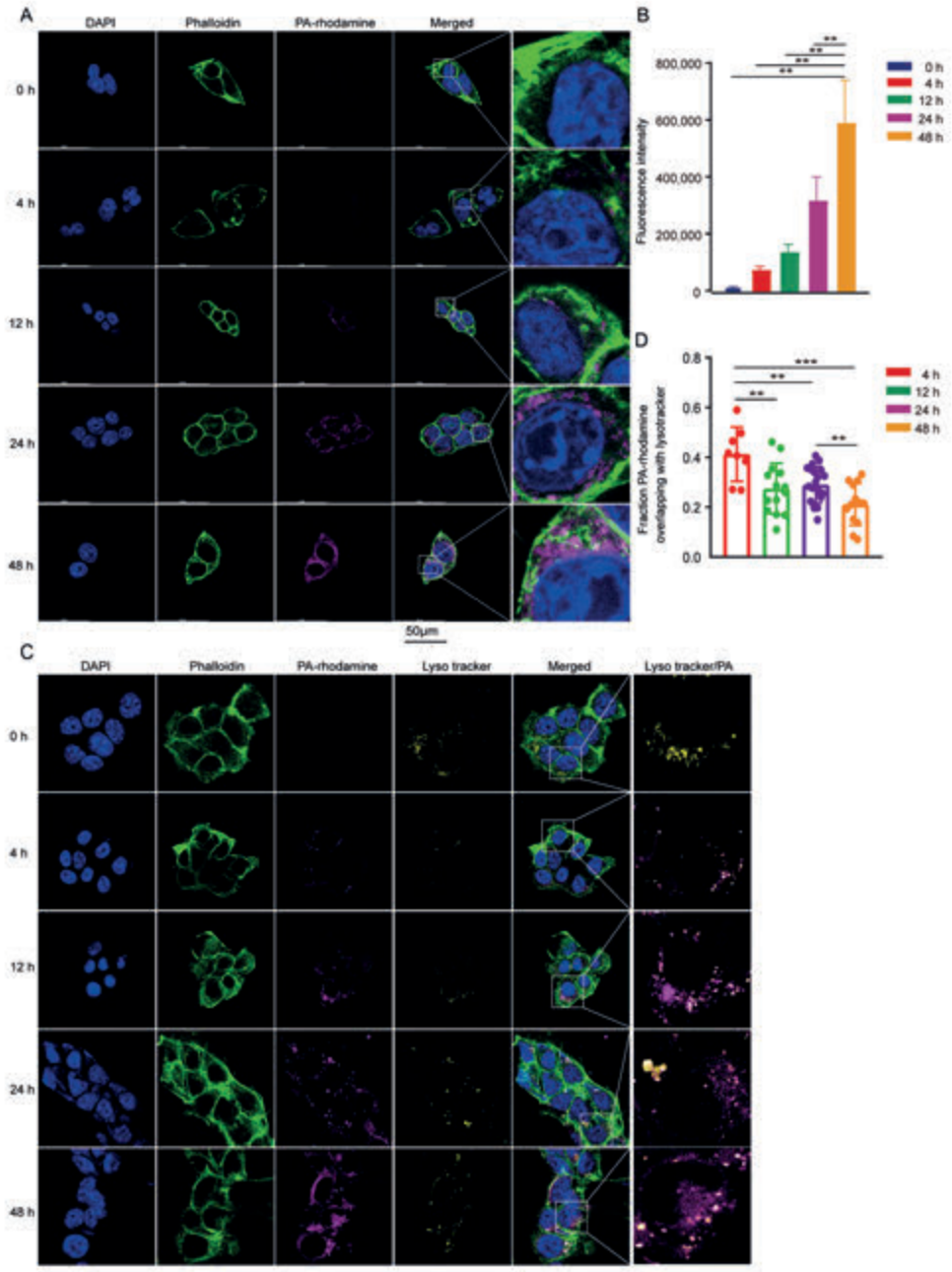

Figure 4. Uptake and intracellular distribution of PA in 4T1 cells. (A) Representative CLSM images of 4T1 cells incubated with PLGA-PA-rhodamine NPs for 1, 4, 12, 24 and 48 h. DAPI, blue; Phalloidin, green; PA-rhodamine, magenta. (B) The average fluorescence intensity of the PA-rhodamine signal was quantified by ImageJ. (C)

Representative CLSM images of 4T1 cells incubated with PLGA-PA-rhodamine NPs for 1, 4, 12, 24 and 48 h and co-stained with LysoTracker. DAPI, blue; Phalloidin, green; PA-rhodamine, magenta; LysoTracker, yellow. (D) Colocalization between PA-rhodamine and LysoTracker as determined by the Mander's colocalization coefficient using ImageJ. Results are representative of multiple cells in one independent experiment. All *p*-values were generated using Student's *t*-test. ** $p \leq 0.01$, *** $p \leq 0.001$.

3.5 PLGA-PA NPs induce reprogramming of TAMs

To assess whether PLGA-PA NPs could induce repolarization of M2 macrophages towards the anti-tumorigenic M1 type, similar as reported for free PA [19,20], RAW 246.7 cells were differentiated towards M2 macrophages, and the expression of M2 and M1 macrophage markers was assessed by flow cytometry after NP uptake (Fig. 5A-C). CD163 is one of the common M2 markers, while CD68 and CD86 are highly expressed on M1 macrophages [41,42]. As shown in Figure 5A, the expression of CD163 greatly reduced in M2 differentiated RAW 246.7 cells upon treatment with PLGA-PA NPs, compared to the group treated with control NPs as well as untreated cells (Fig. 5A). Similarly, the expression of CD68 and CD86 increased upon treatment with PLGA-PA NPs, compared to the control group and untreated M2-differeniated cells (Fig. 5B-C). In line with flow cytometry plots, analysis of the geometric mean showed a significant decrease of CD163 expression and concomitant increase in CD68 and CD86 signal, compared to control groups (Fig. 5D-F). In summary, our results confirm that, similar to free PA, encapsulated PA could partially reverse the M2 phenotype in M2-differeniated RAW 246.7 cells towards the anti-tumorigenic M1 type.

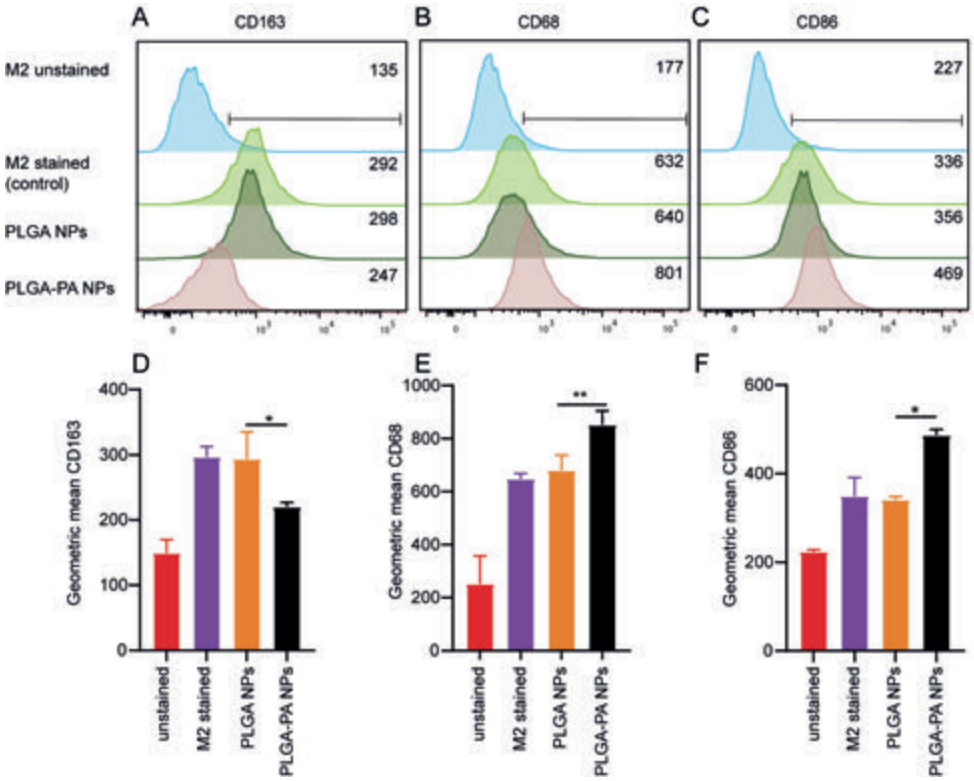

Figure 5. PLGA-PA NPs promote repolarization of M2 macrophages. RAW 264.7 cells were differentiated towards the M2 type by addition of IL-4 to the culture medium, and treated with control PLGA-NPs or PLGA-PA NPs for 48 h. Representative flow cytometry plots of M2 differentiated RAW 264.7 cells stained for the M2 marker (A) CD163, and the M1 markers (B) CD68 and (C) CD86. Analysis and quantification of the geometric mean of the (D) CD163, (E) CD68, and (F) CD86 signals. The *p*-values are for the experimental group compared to M2 (RAW 264.7 cells + IL-4). All data are mean ± SD of three independent experiments, * $p \leq 0.05$, ** $p \leq 0.01$ by a Student's *t*-test.

3.6 PA inhibits 4T1 cell migration and invasion *in vitro*

To explore the effect of PA-containing NPs on 4T1 cell migration and invasion, we performed a wound healing assay (Fig. S2). To this end, the cells were incubated with different PLGA NP formulations for the 48 h duration of the assay (Fig. S2A). The wound healing rates showed that after 12 h, a reduction in wound healing rate in the PLGA-PA NP-treated group became apparent, compared to the control PLGA NP-treated and untreated 4T1 cells (Fig. S2A). At endpoint, we observed

in the untreated and control PLGA NP-treated 4T1 cells a wound healing rate of 86.49% and 73.36%, respectively, whereas the relative wound density was only 43.28% in the PLGA-PA NP-treated group and 31.33% in the PLGA-PA-DOX NP-treated group (Fig. S2B). In addition, we determined the effect of PLGA-PA NPs on the growth and proliferation of 4T1 cells *in vitro* in a colony formation assay (Fig. S2C-D). The results showed that the PA-loaded NPs significantly inhibited the number and size of 4T1 colonies, indicating that PA inhibited the proliferation of 4T1 cells. Importantly, as shown in our MTS results, the PLGA-PA NP concentrations used in the wound healing and colony assays did not induce cellular toxicity (Fig. 2D), thus, the reduction in 4T1 invasive properties, colony numbers and size could not be attributed to adverse cytotoxic effects of PA. These results are consistent with our previous study on the effect of free PA and 4T1 cell invasion [20], demonstrating the ability of PA-loaded NPs to significantly inhibit the invasive properties of 4T1 cells *in vitro*.

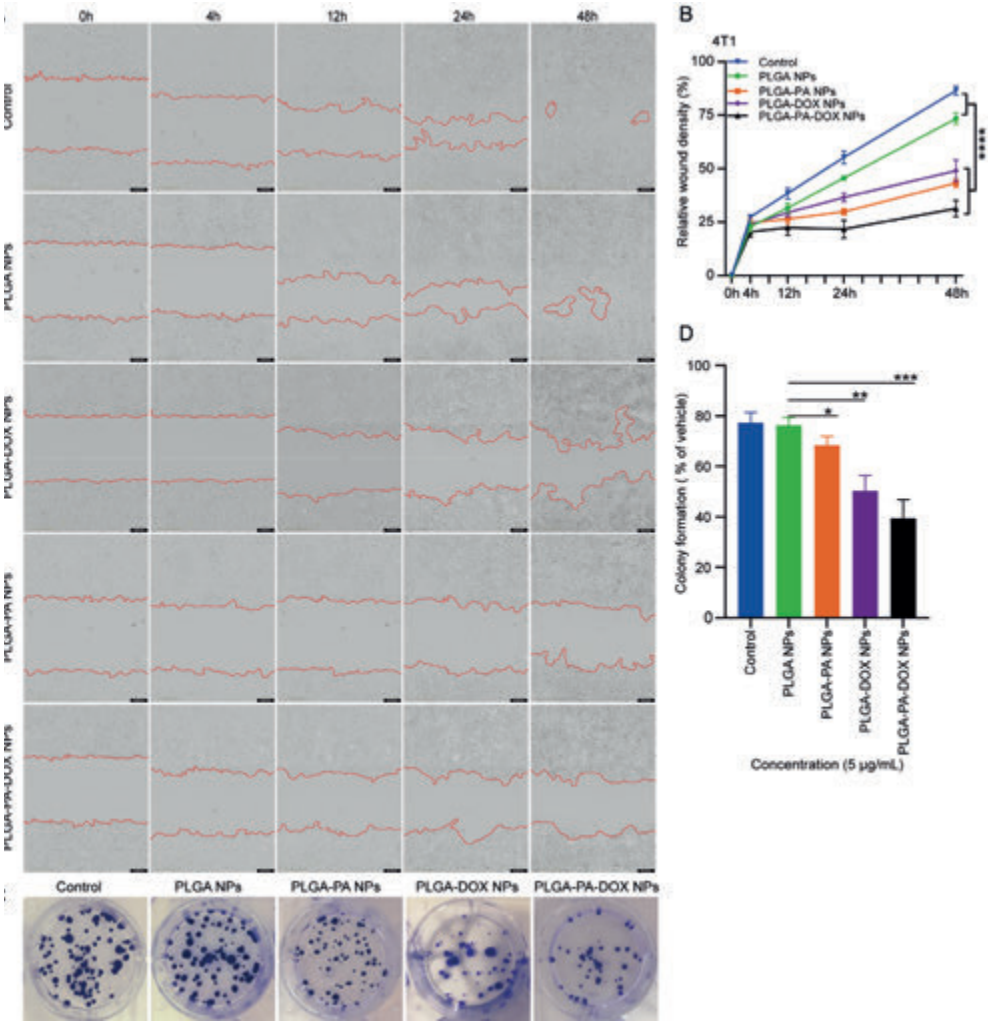

Supplementary Figure 2. PLGA-PA NPs inhibit the migration and invasion of 4T1 cells. (A) The wound healing assay was performed in the presence of 20 µg/mL of PLGA-NPs for 48 h, or in untreated control cells, to determine the invasive properties of 4T1 cells. (B) The images of the wound area were recorded with the Incucyte system, and the relative wound healing rates were calculated after 0, 4, 12, 24 and 48 h. (C) Representative image of 4T1 colonies treated with 5 µg/mL of PLGA-NPs or untreated cells, stained with Giemsa solution. (D) Quantification of the mean cell colony number. Data are means ± SD of three independent experiments. * $p \leq 0.05$, ** $p \leq 0.01$, *** $p \leq 0.001$, **** $p \leq 0.0001$ compared to control.

3.7 PLGA-PA NPs inhibit breast tumor growth *in vivo*

Next, the anti-tumor efficacy of PLGA-PA NPs was assessed in an orthotopic murine breast cancer model. On day 1, 1×10^6 4T1 cells were inoculated into the fourth mammary pad of the mice. The first injection of NPs was administered intratumorally on day 3, and repeated every 5 days for a total of 15 days, and the experiment was terminated on day 18 (Fig. 6A). As shown in Fig. 6B−C, tumor growth was significantly inhibited in the experimental groups treated with free DOX, PLGA-DOX NPs, PLGA-PA NPs and PLGA-PA-DOX NPs, compared to the saline-injected control group. The tumor growth curves showed that PLGA NPs containing PA and/or DOX had a similar effect to free DOX. Free DOX reduced the tumor volume to 62.4 mm^3, while tumor volumes of the untreated and PLGA NP-treated groups were 370.032 mm^3 and 205.258 mm^3, respectively. In the PLGA-PA NP and PLGA-PA-DOX NP-treated groups, the tumor volume was reduced to 34.712 mm^3 and 27.657mm^3, respectively. Comparing the free DOX and PLGA-DOX NPs treatment groups, little difference was found in terms of tumor volume ($p > 0.05$), indicating that both conditions were equally efficient. There was no significant difference between the control groups injected with saline or blank PLGA NPs. Similar, the results of the tumor weight measurements at endpoint showed a significant reduction in tumor weight in the DOX-, PLGA-DOX NP-, PLGA-PA NP- and PLGA-PA-DOX NP-treated groups, compared to the saline-treated group (Fig. 6D). In addition, we found significant differences between the PLGA-PA NP- and PLGA-PA-DOX NP-treated groups, compared to blank PLGA NPs and to the free DOX group (Fig. 6D). These data suggest that PLGA NPs containing PA as single modality had a similar anti-tumor effect as DOX-containing NPs (Fig. 6C). At endpoint, we also determined the blood leukocyte count of the mice to investigate whether the treatment had any detrimental effect on the immune system (Fig. 6E). Our results showed a significantly lower number of leukocytes in the DOX-treated groups, when compared to the control groups treated with saline and blank PLGA NPs. This is a common side effect of chemotherapeutic treatments. Interestingly, the reduction in leukocyte count in the PLGA-PA NP-treated group was less pronounced than after DOX treatment, despite similar treatment efficacies. This might suggest that PA applied alone has less profound systemic side effects than DOX.

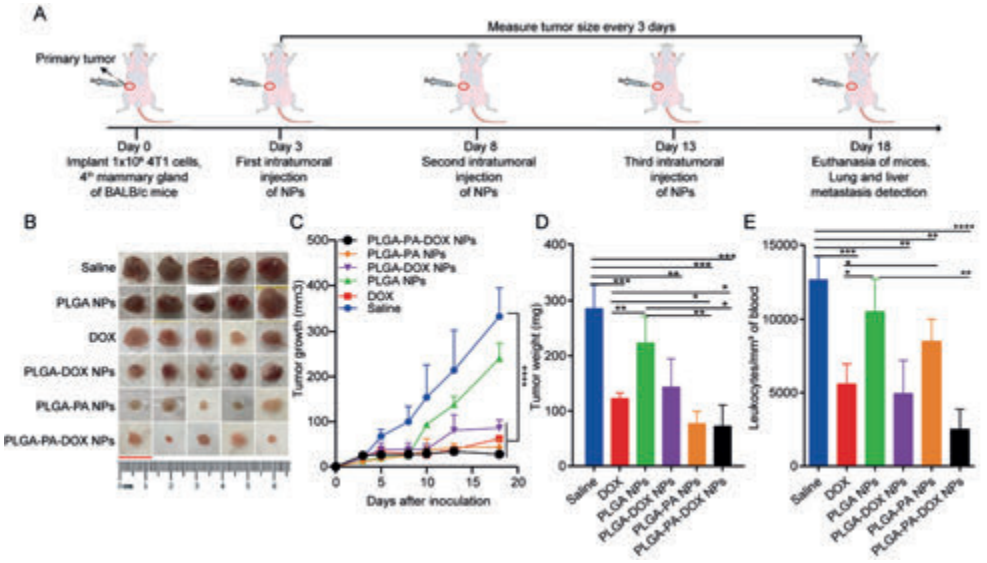

Figure 6. *In vivo* experiments in BALB/c mice bearing 4T1 breast tumors. (A) Experimental timeline: 1 × 10^6 4T1 cancer cells were implanted at the mammary site (day 0) and mice were treated with saline, free DOX, blank PLGA NPs or PLGA NPs loaded with DOX and/or PA by intertumoral injection of NPs for 15 days (6 mice per group) on days 3, 8, and 13 of the experiment, respectively. (B) Photographs of tumors taken from mice carrying 4T1 tumors at the endpoint (day 18). (C) Growth curves of in situ mammary tumors in BALB/c mice showing reduction in tumor volume after treatment with PLGA-PA NPs and DOX-loaded PLGA-PA NPs as well as free DOX. (D) Mean weight of tumors at the endpoint (n = 6). (E) Blood leukocytes count of mice treated with different NP formulations. Data represent mean ± SEM; ** $p \leq 0.01$, *** $p \leq 0.001$, **** $p \leq 0.0001$ by a Student's t-test.

3.8 PLGA-PA NPs inhibit breast cancer metastasis

The 4T1 breast cancer cell line has been reported to be poorly immunogenic and highly susceptible to spread to distant organs, which is associated with a high degree of metastatic properties [43]. Therefore, the effect of the different NP formulations on 4T1 tumor metastasis was evaluated *in vivo*. To this end, we performed a histological study of the liver and lung of all mice, and scored the sections according to the presence of metastasis. In all experimental groups, we could see that the tumor cells infiltrated the liver (arrows, Fig. 7A). In contrast to the control groups (saline and PLGA NPs), the number of metastatic niches and tumor

areas appeared to be smaller in the groups treated with free DOX as well as PLGA NPs containing DOX and/or PA (Fig. 7A, C), ** $p \leq 0.01$, *** $p \leq 0.001$). Next, we compared the number of metastatic niches in the lung tissue of the mice in each group and found that the experimental groups treated with DOX or PLGA NPs containing DOX and/or PA, had significantly fewer metastases in the lung than in the control groups (Fig. 7B, C, *** $p \leq 0.001$). Our results indicate that free DOX as well as PLGA NPs containing DOX and/or PA significantly inhibited the formation of metastasis in the liver and the lung.

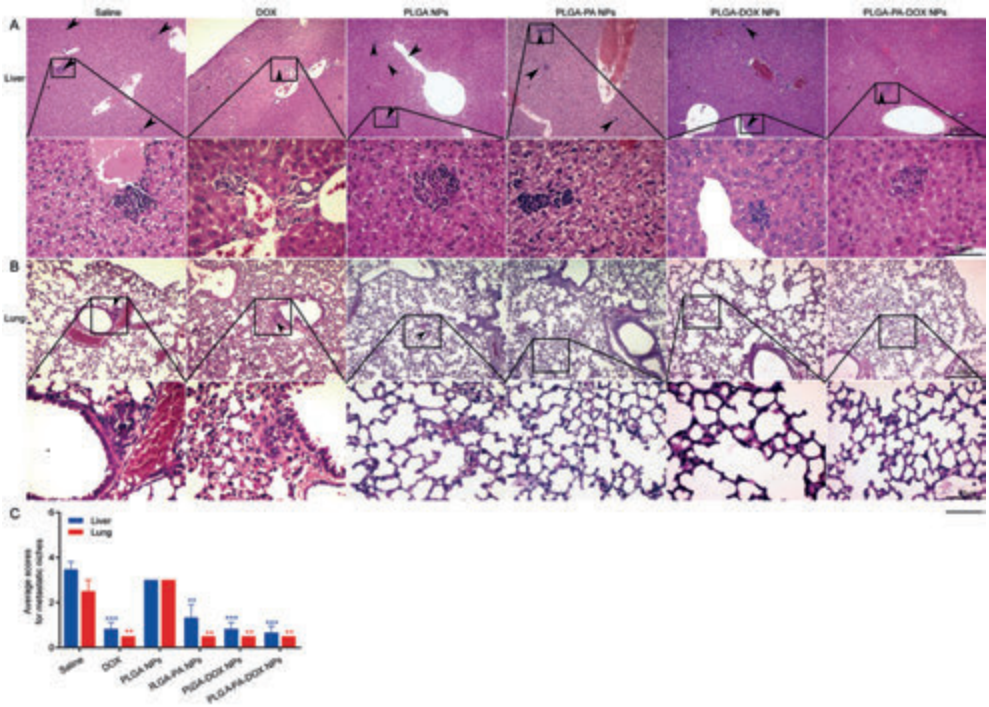

Figure 7. Evaluation of metastatic ecological niches in the lung and liver of mice. Tumor cell migration to secondary sites was observed in the (A) liver and (B) lung. Arrows indicate the presence of metastatic niches. (C) Metastatic niches in the liver and lung were assessed semi-quantitatively. Immunostaining images were magnified 400×. All data are expressed as the mean ± SD of six independent values (n = 6) for each group. ** $p \leq 0.01$, *** $p \leq 0.001$. scale bars of 100× = 100 μm, scale bars of 400× = 25 μm.

3.9 Gene and protein expression profiles in TME

To assess the effect of the different PLGA NP formulations on the breast TME, with respect to apoptosis, cell survival, drug resistance and immune regulation, we performed immunohistochemistry (IHC) and RT-qPCR analysis of the tumors at the endpoint. As shown in Figure 8A, pro-apoptotic protein caspase-3 protein was significantly upregulated after treatment with free DOX, as well as PLGA-DOX NPs and PLGA-PA-DOX NPs (** $p \leq 0.01$, *** $p \leq 0.001$, **** $p \leq 0.0001$), indicating the induction of apoptosis in response to DOX. Interestingly, the expression of pro-apoptotic protein caspase-3 in the PLGA-PA-DOX NP group (H-score: 160.33 ± 30.44) was 1.84-fold higher (* $p \leq 0.05$) than in the free DOX group (H-score: 87 ± 6.08) and 1.23-fold higher than in the PLGA-DOX NP group (H-score: 130.83 ± 16.00; Fig. 8B), suggesting an additive effect of PA and DOX in inducing tumor cell apoptosis. In addition, RT-qPCR results showed that the expression of the apoptosis-related genes *Fadd* and *Apaf-1* was significantly upregulated upon treatment with free DOX, PLGA-DOX NPs and PLGA-PA-DOX NPs (* $p \leq 0.05$, ** $p \leq 0.01$, *** $p \leq 0.001$, **** $p \leq 0.0001$), and PLGA-PA NPs alone were able to induce upregulation of *Apaf-1* (Fig. 8C-D). In addition, the expression of the apoptosis inhibitor *Birc5* (also known as Survivin) was significantly reduced in response to PLGA-DOX NPs, PLGA-PA NPs, and PLGA-PA-DOX NPs (** $p \leq 0.01$, *** $p \leq 0.001$, **** $p \leq 0.0001$; Fig. 8E). Interestingly, the drug resistance gene multidrug resistance 1 (*Mdr1*) was significantly reduced in response to PLGA-DOX NPs, PLGA-PA NPs, and PLGA-PA-DOX NPs (** $p \leq 0.01$, *** $p \leq 0.001$, **** $p \leq 0.0001$), indicating that delivery of PA alone can reduce *Mdr1* expression (Fig. 8F). Interestingly, when free DOX was applied, the expression of drug resistance gene *Mdr1* was significantly increased, but this effect could not be seen when DOX was encapsulated inside of PLGA NPs, suggesting that encapsulation prevents the development of drug resistance. In summary, our results show that PLGA-PA NPs alone increased the expression *Apaf-1*, but not caspase-3, and reduced the expression of the cell survival gene *Birc5* and drug resistance gene *Mdr1*, suggesting a powerful role of PA in the modulation of the breast TME. Importantly, our data showed that, when combined, DOX and PA could act in concert in further increasing tumor cell apoptosis and in reducing drug resistance.

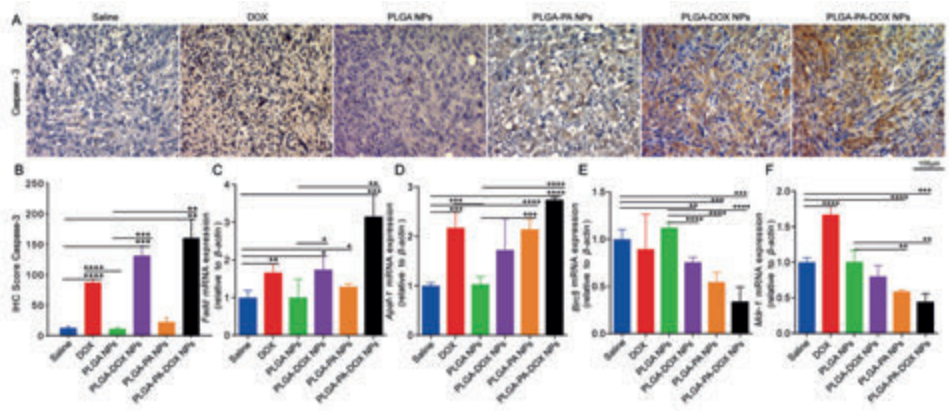

Figure 8. Assessment of cell death, survival and drug resistance in the TME after NP treatment. (A) Immunostaining and (B) scoring of caspase-3 signal. Immunostaining images were magnified 100×. The score of each image was analyzed, and the data was summarized into a histogram. Scale bar is indicated. mRNA expression of (C) *Fadd*, (D) *Apaf-1*, (E) *Birc5* and (F) *Mdr-1* in tumors after NP treatment relative to *β-actin*. All data are expressed as mean ± SD, * $p \leq 0.05$, ** $p \leq 0.01$, *** $p \leq 0.001$, **** $p \leq 0.0001$.

Next, we assessed the expression of *Nfκb*1, matrix metalloproteinase 2 (*Mmp2*) and C-X-C motif chemokine 12 (*Cxcl12*) in the TME by IHC and RT-qPCR analysis. As shown in Figure 9, the expression of the transcription factor *Nfκb*1 and the metalloproteinase *Mmp2*, which promote cancer invasion and angiogenesis, and the *Cxcl12* gene, which promotes the proliferation, survival, and invasion of cancer cells, were significantly downregulated in the TME in response to treatment with free DOX, PLGA-DOX NPs and PLGA-PA-DOX NPs, compared to the control groups (Fig. 9A–D). Interestingly, PLGA-PA NPs alone also downregulated the expression of *Nfκb*1, while it did not affect *Cxcl12* expression. Furthermore, RT-qPCR results showed that the expression of invasion and metastasis-related genes *Mmp2* and *Cxcl12* were significantly down-regulated (* $p \leq 0.05$, ** $p \leq 0.01$) after treatment with free DOX, PLGA-DOX NPs and PLGA-PA-DOX NPs (Fig. 9E–F), in agreement with the IHC data. In contrast, PLGA-PA NPs alone were able to downregulate *Mmp2* without affecting *Cxcl12* expression (Fig. 9E–F). In addition, we examined the effect of NPs on *Mmp2* and *Cxcl12* expression at the cellular level by RT-qPCR. The results showed that the expression of both invasion- and metastasis-related genes *Mmp2* and *Cxcl12* were significantly down-regulated after treatment with free DOX, free PA, PLGA-DOX NPs, PLGA-PA NPs and PLGA-PA-DOX NPs (Supplementary Fig. 3A–B). In summary, these results highlight that, at the molecular level, the reduction in breast tumor growth and metastasis upon

treatment with PA and DOX are mediated via different signaling pathways. When DOX and PA are combined, both pathways were affected simultaneously.

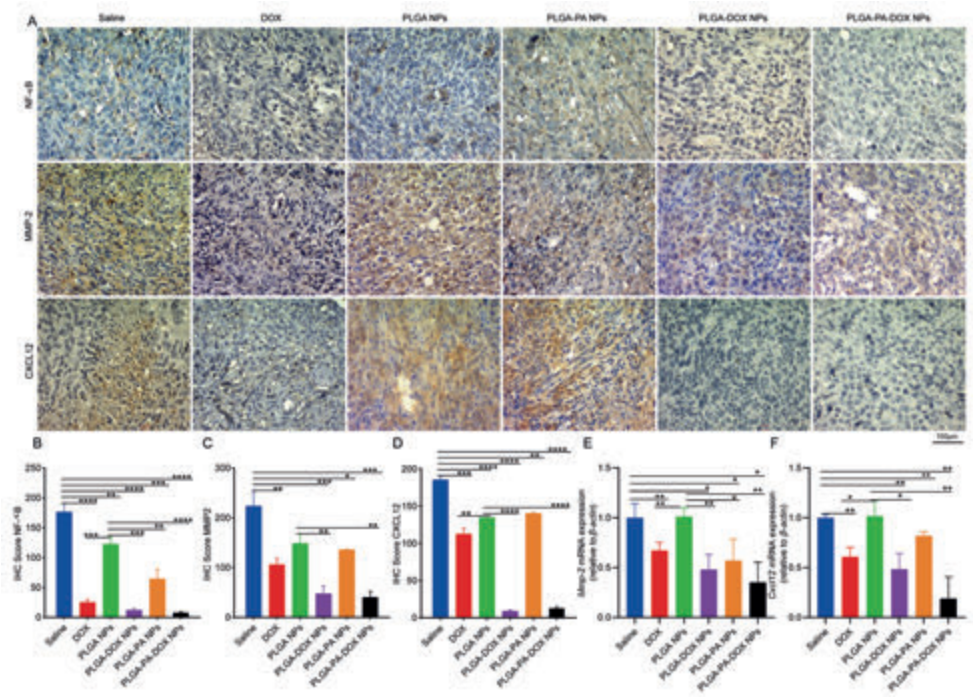

Figure 9. Assessment of intracellular signaling pathways involved in cancer invasion, angiogenesis and proliferation in the TME. (A) *Nfkb*, *Mmp2* and *Cxcl12* immunostainings were performed on tumor sections from mice at endpoint. (B-D) Semi-quantitative scoring of *Nfkb*, *Mmp2* and *Cxcl12* signals in tumor sections at endpoint. mRNA expression of (E) *Mmp2* and (F) *Cxcl12* in tumors after NP treatment relative to *β-actin*. All data are expressed as mean ± SD, * $p \leq 0.05$, ** $p \leq 0.01$, *** $p \leq 0.001$, **** $p \leq 0.0001$.

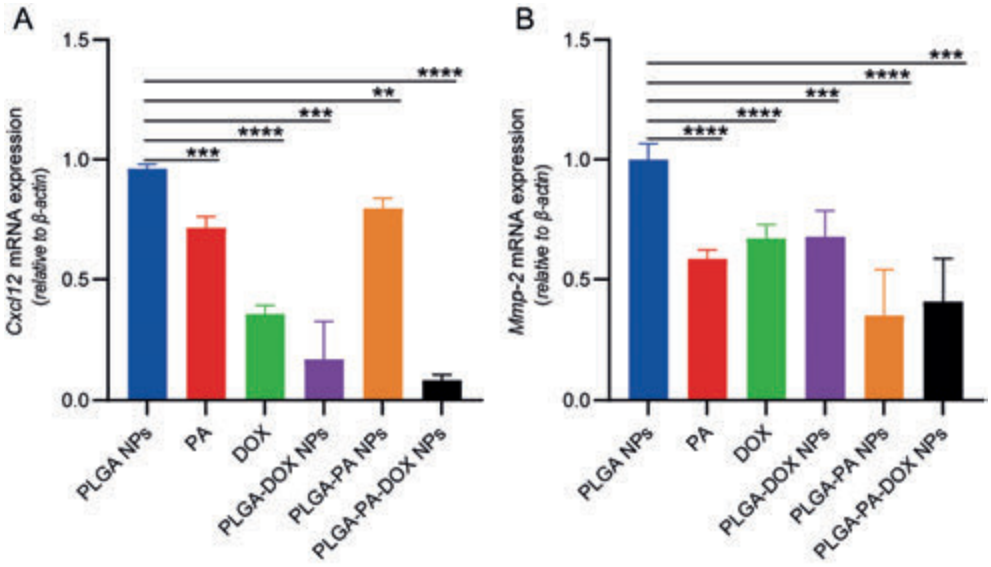

Supplementary Figure 3. Assessment of intracellular signalling pathways involved in invasion, angiogenesis and proliferation of 4T1 cells. 4T1 cells were treated with 65.4 µg/mL of NPs (equivalent to 7.5214 µg/mL free DOX and 32.7 µg/mL free PA), control NPs, free DOX (7.5214 µg/mL) and free PA (32.7 µg/mL). The mRNA expression of *Mmp2* (A) and *Cxcl12* (B) in 4T1 cells relative to *β-actin* after 48 h incubation. All data are expressed as mean ± SD, ** $p \leq 0.01$, *** $p \leq 0.001$, **** $p \leq 0.0001$.

Finally, the immunomodulatory effect of the different PLGA-NP-formulation on the TME and in particular TAMs was assessed by IHC. We found that compared to the control groups (saline and PLGA NPs), the expression of the M2 TAM marker CD163 was downregulated in the groups treated with free DOX, PLGA-DOX NPs, PLGA-PA NPs, and PLGA-PA-DOX NPs. However, the effect was most prominent in the DOX-treated groups (Fig. S4A and C). Similarly, the expression of the M1 macrophage marker CD68 was highly upregulated upon treatment with DOX and PLGA DOX NPs, and (to a lesser but significant extent) PLGA-PA-DOX NPs (Fig. S4B and D).

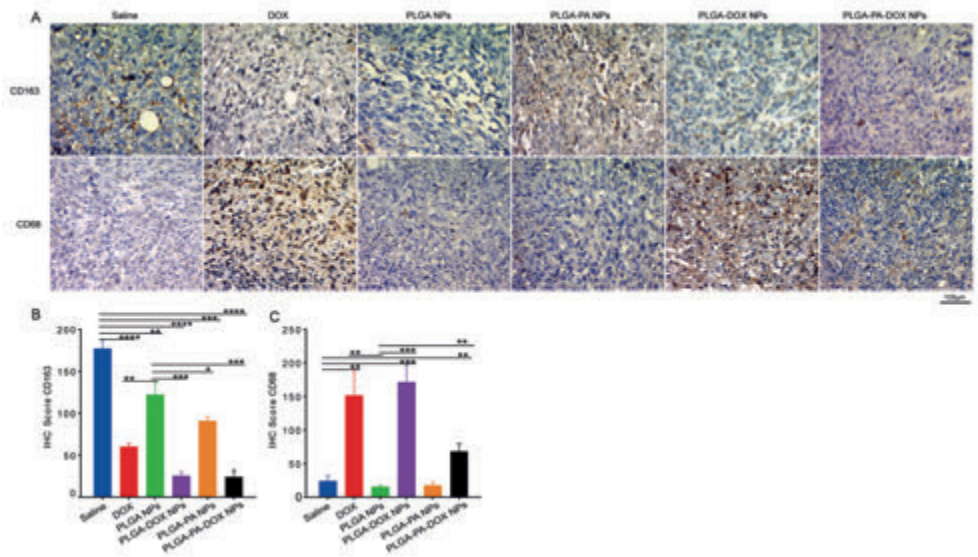

Supplementary Figure 4. Reduction of the immunosuppressive TME after treatment. 4T1 breast tumor tissues isolated from mice treated with saline, free DOX or different PLGA NP formulations were stained for TAM markers. (A) Representative images of CD163- and CD68-stained tumor sections. Scale bar is indicated. Semi-quantitative scoring of (B) CD163 and (C) CD68 signals in tumor sections at endpoint. The score of each image was analyzed and plotted as a histogram. All data are expressed as mean ± SD, * $p \leq 0.05$, ** $p \leq 0.01$, *** $p \leq 0.001$, **** $p \leq 0.0001$.

3.10 PLGA-PA NPs induce lymphocyte infiltration in breast tumors

To further analyze the effect of PA on 4T1 breast tumor architecture, we carefully inspected H&E-stained sections of untreated, free DOX- and NP-treated tumors. Visual inspection of the tumor sections confirmed the presence of morphological characteristics indicative of neoplastic cells, tumor necrosis and lymphocyte infiltration in all treatment groups (Supplementary Fig. 5). Overall, we found a denser network of tumor cells in the saline- and PLGA-NP-treated control groups, compared to the groups treated with free DOX, PLGA-DOX NPs, PLGA-PA NPs and PLGA-DOX-PA NPs, suggesting disintegration of the TME as a result of advanced necrosis in response to treatment (Fig. 10A).

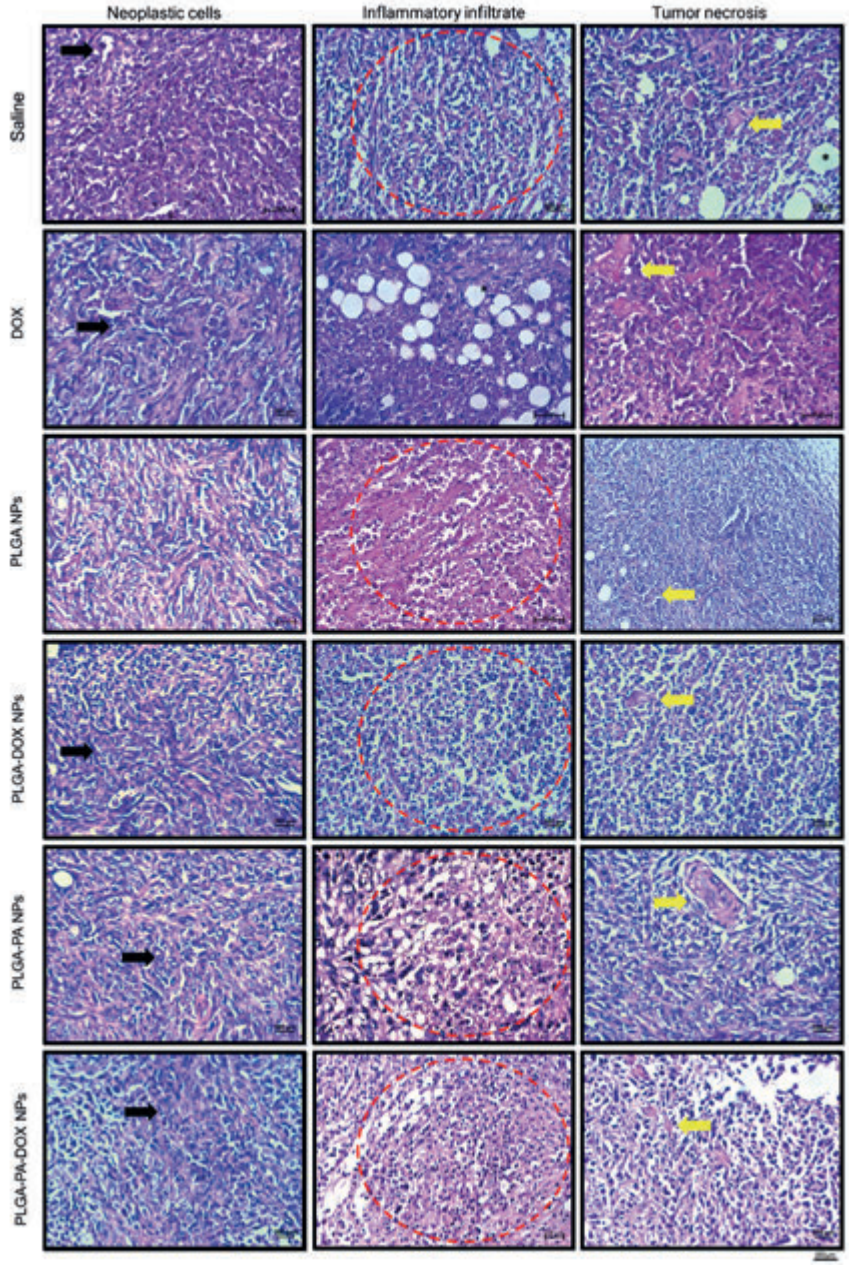

Supplementary Figure 5. Representative images of H&E-stained mammary tumors of mice treated with saline, free DOX, PLGA-DOX NPs, PLGA-PA NPs and PLGA-PA-DOX NPs, showing morphological characteristics of neoplastic cells (black arrow), lymphocyte infiltrates (red dashed circle) and areas of tumor necrosis (yellow arrow). Scale bars are indicated.

To quantify these changes, the occurrence of areas of necrotic cells and infiltrating lymphocytes within each section were scored as < 15%, 15−25%, 25−50%, > 50% of the total section area (Fig. 10). Tumor necrosis and in particular the presence of necrotic foci, is often associated with aggressive tumor development and metastasis and is thought to be an important indication of poor prognosis in breast cancer [44]. Our results demonstrated that 50% of the tumor sections of untreated mice as well as mice treated with either control PLGA NPs, PLGA-DOX NPs or PLGA-PA-DOX NPs showed the presence of large areas of necrotic cells, while treatment with PLGA-PA NPs led to a significant reduction in necrosis (Fig. 10A, B). In addition, visual inspection showed an increase in lymphocyte infiltration in the PA-treated groups (Fig. 10A, C). The presence of tumor-infiltrating lymphocytes predicts increased survival, which has been associated with an anti-tumor immune response and improved prognosis in breast cancer [45]. Analysis of tumor-infiltrating lymphocytes demonstrated that 80−90% of untreated tumors, or tumors treated with either control PLGA NPs, PLGA-DOX NPs or free DOX had a lymphocyte content of less than 25%. This was significantly increased in PLGA-PA-DOX NP-treated tumors, with 50% of tumors sections showing 25−50% of infiltrating lymphocytes. When the mice were treated with PLGA-PA NPs, 80% of the sections showed a lymphocyte content of more than 50%. In addition, in PLGA-PA NP- and PLGA-PA-DOX NP-treated tumors we observed a preferential localization of lymphocytes in necrotic tumor areas, while we did not observe this in the other treatment groups. These results suggest that, in contrast to free and encapsulated DOX, PA in form of PLGA-PA NPs and PLGA-PA-DOX NPs displays immunomodulatory properties by increasing the presence of lymphocytes in the tumor.

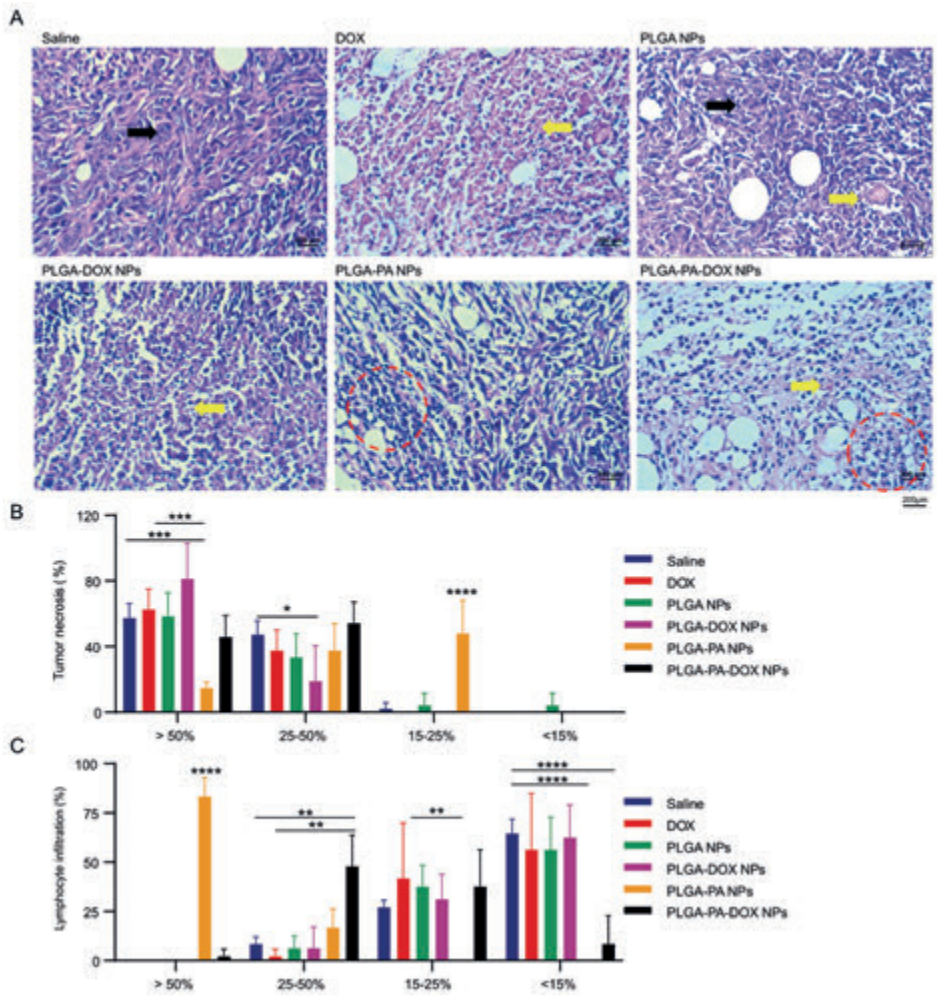

Figure 10. (A) Representative images of H&E-stained mammary tumor sections of mice treated with saline, free DOX, PLGA-DOX NPs, PLGA-PA NPs or PLGA-PA-DOX NPs. (B) The percentage of necrotic areas, quantified in H&E-stained tumor sections. (C) The percentage of lymphocytic infiltration, quantified in H&E-stained tumor sections. Nuclei (blue-purple), and extracellular matrix and cytoplasm (pink). Scale bars are indicated. Black arrows indicate neoplastic cells; yellow arrows indicate areas of extensive necrosis; red dashed circles indicate areas with lymphocytic infiltration. Data are expressed as percentages ± SD, * $p \leq 0.05$, ** $p \leq 0.01$, *** $p \leq 0.001$, **** $p \leq 0.0001$.

4 Discussion

It is well known that chemotherapeutic agents, such as DOX, display anti-tumor effects and significantly reduce tumor size in breast cancer models [46-50]. However, the risk of drug resistance, disease reoccurrence and a broad spectrum of adverse side effects remain a major concern. To overcome these limitations, researchers seek to find novel drug combinations for the treatment of breast cancer. To the best of our knowledge, we here describe a novel approach combining PA and DOX in a PLGA-based NP platform. The anti-tumor effects of PLGA-PA NPs and PLGA-PA-DOX NPs were validated *in vitro* and *in vivo* in an orthotopic murine breast cancer model. Our results showed that NPs loaded with PA, as well as PA and DOX, effectively inhibited breast tumor growth and metastasis. Strikingly, the therapeutic effect of PLGA-PA NPs was similar to PLGA-DOX NPs, PLGA-PA-DOX NPs and free DOX. Moreover, in addition to the effects of PLGA-DOX NPs and free DOX, PA-containing NPs increased the number of tumor-infiltrating lymphocytes, indicative of an anti-tumor immune response. Thus, PLGA-PA NPs, as monotherapy or in combination with DOX, potentially represent a promising novel nanoformulation for breast cancer therapy (Scheme 1).

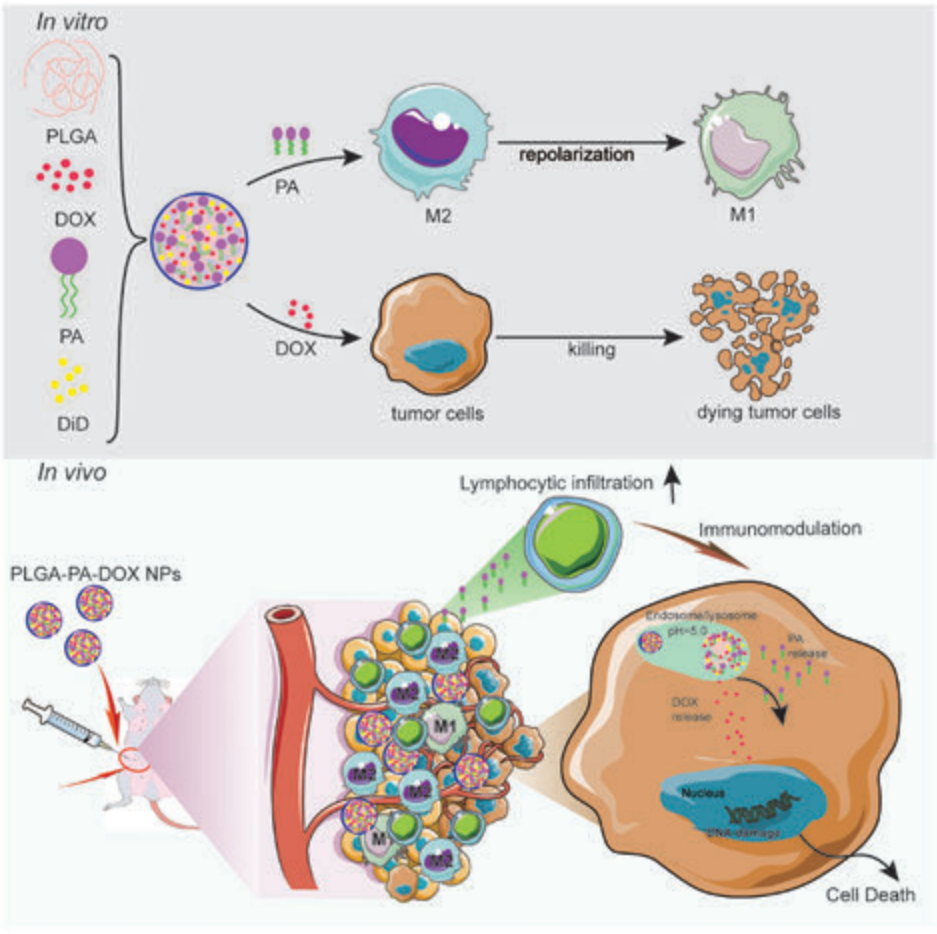

Scheme 1. Schematic illustration of the therapeutic actions of PLGA-PA and PLGA-PA DOX NPs on 4T1 breast cancer cells *in vitro* and *in vivo*.

To encapsulate PA and/or DOX together into PLGA NPs, we used a double emulsion-solvent-evaporation method, which has been shown to improve drug delivery *in vivo* and to reduce drug side effects [51,52]. Encapsulated DOX followed the typical release profile from NPs with an initial burst followed by a period of sustained release [53,54]. In contrast to DOX, the release of PA was incomplete and slower, but sustained for a prolonged period. We speculate that due the lipophilic nature of the saturated FA, PA was maintained for longer time in the hydrophobic core of the PLGA NPs. Our microscopy study confirmed the release profiles of PA and DOX after cellular uptake of PLGA-PA NPs and PLGA-DOX

NPs. Initially, the intracellular concentrations of DOX and PA were low, in contrast to free DOX, which readily diffused via the membrane to the nucleus [30,55]. The difference between free and encapsulated DOX was due to the initial slow NP uptake, which then increased over time. With increasing NP uptake, encapsulated DOX was readily released intracellularly. In contrast to DOX, the intracellular release of PA was slower and PA accumulated in the cytoplasm, indicating that DOX and PA exert their actions via different kinetics and subcellular compartments.

In line with our previous study using free PA [20], PLGA-PA NPs significantly inhibited the invasive and proliferative properties of 4T1 cells *in vitro*. Our *in vivo* results demonstrated that PA inhibited tumor growth with the same efficacy as free DOX and PLGA-DOX NPs. Our findings were consistent with other studies reporting inhibition of tumor growth after treatment with free PA in colorectal, liver, prostate and breast cancer cells [19-24]. Similar to our approach, Feng *et al*. recently used PA-modified human serum albumin NPs loaded with pirarubicin to effectively deliver PA to murine breast tumors and M2 macrophages *in vivo*. In line with our results, the authors reported inhibition of breast cancer growth and almost no remaining metastasis after treatment with PA-modified albumin NPs [25]. This underlines the potential of PA as novel agent for the effective treatment of breast cancer. However, the underlying molecular actions of PA remain largely elusive. A study by Baumann *et al*. showed that PA activated the endoplasmic reticulum stress response in breast cancer cells, leading to cell cycle delay and inhibition of tumor growth [56]. Generally, there are two main sources of FAs for mammalian cells, exogenously-derived (dietary) and endogenously synthesized FAs. The membrane composition is altered in a variety of cancers, due to epigenetic changes that affect the cellular FA synthesis [57,58]. This has been linked to changes in cancer cell membrane fluidity and the development of drug resistance. One hypothesis is that exogenously applied FAs can insert into the membrane of cancer cells and reverse membrane fluidity and/or cellular functions [59], or act as membrane disrupting agent that induce cytotoxicity. Another hypothesis is that exogenously applied FAs incorporate into more complex lipids, as shown for PA in cancer cells [60]. Our microscopy data has shown that intracellular delivered PA-rhodamine accumulated in the cytoplasm within the first 48 h after NP uptake, suggesting that encapsulated PA exerts its cytotoxic effect towards cancer cells via intracellular pathways rather than by incorporating into the plasma membrane.

While PLGA-PA NPs and PLGA-DOX NPs both reduced tumor growth and metastasis *in vivo*, molecular analysis of the tumors after treatment with PLGA-PA NPs and PLGA-PA-DOX indicated that PA and DOX act via different molecular pathways. Free DOX, PLGA-DOX NPs and PLGA-PA-DOX NPs significantly

promoted the expression of several apoptosis-related genes in cancer cells. PLGA-PA NPs promoted apoptosis via a caspase-3-independent pathway, and effectively induced the expression of *Apaf-1* and downregulated *Birc5* (Survivin) expression. In line with these findings, previous results demonstrated that PA promoted apoptosis by inducing a G1 phase block in the cell cycle [24,61].

Furthermore, our results showed that treatment of 4T1 cells with free DOX increased the expression of *Mdr1*, in accordance with the notion that DOX leads to the development of drug resistance [62,63]. In contrast to free DOX, PLGA-DOX NPs did not upregulate *Mdr1* expression, illustrating that drug resistance could be effectively suppressed by nano-delivery systems, as shown also by other groups [30,64,65]. Similar to our results, it has previously been shown that DOX conjugated to PA significantly inhibited tumor growth and suppressed *Mdr1* expression [66].

While our *in vitro* results indicated an additive effect when PA and DOX were co-encapsulated, PLGA-PA-DOX NPs did not further reduce breast cancer growth and invasion *in vivo*, when compared to PLGA DOX NPs and PLGA-PA NPs alone. However, at the molecular level, combinational treatment with PA and DOX further increased apoptosis and reduced drug resistance. On the other hand, the presence of DOX also seemed to counteract the effect of PA. For example, PLGA-PA NPs induced infiltration of lymphocytes into the breast TME *in vivo*, but this was significantly reduced when DOX was co-encapsulated, albeit, the levels were higher than in the PLGA-DOX-NP and the control groups. The presence of tumor-infiltrating lymphocytes in the TME is a favorable prognostic factor and therapeutic predictor [67,68]. Tumor tissues with > 50% lymphocyte infiltration have the best therapeutic outcome when treated clinically [69]. Thus, our findings support the notion that PA regulates the pro-inflammatory response and T-cell function [70]. For example, PA induced an inflammatory response in T cells by modulating the STAT5-PI3K/Akt pathway [71], and a PA-rich diet promoted increased lymphocyte proliferation in rats [72]. We speculate that the reduction in tumor-infiltrating lymphocytes, when DOX was co-encapsulated, might have been caused by the global cytotoxic actions of DOX on cellular subsets in the TME. Notably, our *in vitro* results also demonstrated that PLGA-PA NPs promoted the reversal of M2 macrophages to M1 macrophages, which is in agreement with our previous researches [19,20]. *In vivo*, PLGA-PA NPs and PLGA-PA-DOX NPs significantly reduced the expression of CD163, but only PLGA-PA-DOX NPs concomitantly increased the expression of CD68 in the TME. However, similar significant increases in CD68 were observed in the free DOX and PLGA-DOX NP groups. Thus, whether PA reduced the expression of CD163 by repolarization of existing TAMs, despite of *in vitro* results pointing in that direction, cannot be concluded with

certainty. In mouse mammary tumors, chemotherapy has been reported to deplete immunosuppressive (M2-like) TAMs and to recruit large numbers of macrophages [73]. Newly infiltrating macrophages greatly contributed to breast cancer drug resistance and relapse after chemotherapy [74]. Moreover, when macrophages were treated with tumor-debris of DOX-resistant tumor cells *in vitro*, this favored the expression of CD68 on TAMs [75]. Therefore, while CD68 is regarded as a M1 marker *in vitro* [76], its expression and prognostic value in cancer patients remains controversial. Triple negative breast cancer with a large number of infiltrating CD68-positive TAMs had a high risk of distant metastasis, poor prognosis, low rates of disease-free and overall survival [77]. Based on our data, we speculate that the reduction of CD163 and increase of CD68 expression in the DOX-treated groups might be a result of the chemotherapy. In addition, the lack of increase in CD68 expression after PA treatment might indicate that PLGA-PA NPs did not lead to recruitment of new macrophages (CD68+) to the TME. In summary, while PA seems to reduce the expression of CD163 in the TME, additional research is needed to understand whether PA repolarizes TAMs, in particular in combination with DOX.

While PA was effective in treating 4T1 breast cancer, it is important to remark that also tumorigenic effects of PA have been reported, such as in gastric and pancreatic cancer cells, melanoma and oral carcinomas, where PA significantly promoted metastasis and the invasion potential of cancer cells [78-80]. Also, a link between FA consumption and the onset of breast cancer in obesity has been reported. For example, cellular adaptation to obesity was governed by PA, which led to enhanced tumor formation ability in murine breast cancer cells by inducing epigenetic changes [81]. Likely, these contradictory results reflect the highly heterogenous nature of breast cancer, which is driven by genetic and epigenetic modifications, as well as by the influence of a heterogenous TME. Indeed, Rizzo *et al*. demonstrated that different breast cancer cell lines exhibited different sensitivities to the lipid environment [82]. PA was able to remodel the endoplasmic reticulum membrane and to reduce cell viability of MDA-MB-231 cells, while MCF7 cells were not affected under the same conditions. Metabolic heterogeneity in subtypes of breast cancer has also been observed among patient biopsies [83], and cell lines representing different human breast cancer subtypes [84]. Thus, further studies are needed to elucidate why PA is powerful in treating 4T1 triple negative breast cancer, while promoting tumor growth and metastasis in other subtypes of cancer. An important prerequisite for the clinical application of PA in breast cancer treatment is the identification of patient populations that would benefit from the immunomodulatory properties of PA.

References

1. Masoud, V.; Pages, G. Targeted therapies in breast cancer: New challenges to fight against resistance. World J Clin Oncol 2017, 8, 120-134, doi:10.5306/wjco.v8.i2.120.
2. Wu, T.; Dai, Y. Tumor microenvironment and therapeutic response. Cancer Lett 2017, 387, 61-68, doi:10.1016/j.canlet.2016.01.043.
3. He, Y.; de Araujo Junior, R.F.; Cruz, L.J.; Eich, C. Functionalized Nanoparticles Targeting Tumor-Associated Macrophages as Cancer Therapy. Pharmaceutics 2021, 13, 50, doi:10.3390/pharmaceutics13101670.
4. Lv, R.; Bao, Q.; Li, Y. Regulation of M1type and M2type macrophage polarization in RAW264.7 cells by Galectin9. Mol Med Rep 2017, 16, 9111-9119, doi:10.3892/mmr.2017.7719.
5. Kinaret, P.A.S.; Scala, G.; Federico, A.; Sund, J.; Greco, D. Carbon Nanomaterials Promote M1/M2 Macrophage Activation. Small 2020, 16, e1907609, doi:10.1002/smll.201907609.
6. Xiao, H.; Guo, Y.; Li, B.; Li, X.; Wang, Y.; Han, S.; Cheng, D.; Shuai, X. M2-Like Tumor-Associated Macrophage-Targeted Codelivery of STAT6 Inhibitor and IKKbeta siRNA Induces M2-to-M1 Repolarization for Cancer Immunotherapy with Low Immune Side Effects. ACS Cent Sci 2020, 6, 1208-1222, doi:10.1021/acscentsci.9b01235.
7. Hobson-Gutierrez, S.A.; Carmona-Fontaine, C. The metabolic axis of macrophage and immune cell polarization. Dis Model Mech 2018, 11, doi:10.1242/dmm.034462.
8. Shaikh, S.; Channa, N.A.; Talpur, F.N.; Younis, M.; Tabassum, N. Radiotherapy improves serum fatty acids and lipid profile in breast cancer. Lipids Health Dis 2017, 16, 92, doi:10.1186/s12944-017-0481-y.
9. Cadenas, C.; Vosbeck, S.; Edlund, K.; Grgas, K.; Madjar, K.; Hellwig, B.; Adawy, A.; Glotzbach, A.; Stewart, J.D.; Lesjak, M.S., *et al*. LIPG-promoted lipid storage mediates adaptation to oxidative stress in breast cancer. Int J Cancer 2019, 145, 901-915, doi:10.1002/ijc.32138.
10. Germain, N.; Dhayer, M.; Boileau, M.; Fovez, Q.; Kluza, J.; Marchetti, P. Lipid Metabolism and Resistance to Anticancer Treatment. Biology (Basel) 2020, 9, 21, doi:10.3390/biology9120474.
11. Jiang, N.; Zhang, G.; Pan, L.; Yan, C.; Zhang, L.; Weng, Y.; Wang, W.; Chen, X.; Yang, G. Potential plasma lipid biomarkers in early-stage breast cancer.

Biotechnol Lett 2017, 39, 1657-1666, doi:10.1007/s10529-017-2417-z.

12. Luo, X.; Zhao, X.; Cheng, C.; Li, N.; Liu, Y.; Cao, Y. The implications of signaling lipids in cancer metastasis. Exp Mol Med 2018, 50, 1-10, doi:10.1038/s12276-018-0150-x.

13. Marino, N.; German, R.; Rao, X.; Simpson, E.; Liu, S.; Wan, J.; Liu, Y.; Sandusky, G.; Jacobsen, M.; Stoval, M., *et al*. Upregulation of lipid metabolism genes in the breast prior to cancer diagnosis. NPJ Breast Cancer 2020, 6, 50, doi:10.1038/s41523-020-00191-8.

14. Yoon, S.; Lee, M.Y.; Park, S.W.; Moon, J.S.; Koh, Y.K.; Ahn, Y.H.; Park, B.W.; Kim, K.S. Up-regulation of acetyl-CoA carboxylase alpha and fatty acid synthase by human epidermal growth factor receptor 2 at the translational level in breast cancer cells. J Biol Chem 2007, 282, 26122-26131, doi:10.1074/jbc.M702854200.

15. Guan, X.; Liu, Z.; Zhao, Z.; Zhang, X.; Tao, S.; Yuan, B.; Zhang, J.; Wang, D.; Liu, Q.; Ding, Y. Emerging roles of low-density lipoprotein in the development and treatment of breast cancer. Lipids Health Dis 2019, 18, 137, doi:10.1186/s12944-019-1075-7.

16. Rabold, K.; Aschenbrenner, A.; Thiele, C.; Boahen, C.K.; Schiltmans, A.; Smit, J.W.A.; Schultze, J.L.; Netea, M.G.; Adema, G.J.; Netea-Maier, R.T. Enhanced lipid biosynthesis in human tumor-induced macrophages contributes to their protumoral characteristics. Journal for ImmunoTherapy of Cancer 2020, 8, e000638, doi:10.1136/jitc-2020-000638.

17. Corn, K.C.; Windham, M.A.; Rafat, M. Lipids in the tumor microenvironment: From cancer progression to treatment. Prog Lipid Res 2020, 80, 101055, doi:10.1016/j.plipres.2020.101055.

18. Li, G.; Liu, D.; Kimchi, E.T.; Kaifi, J.T.; Qi, X.; Manjunath, Y.; Liu, X.; Deering, T.; Avella, D.M.; Fox, T., *et al*. Nanoliposome C6-Ceramide Increases the Anti-tumor Immune Response and Slows Growth of Liver Tumors in Mice. Gastroenterology 2018, 154, 1024-1036 e1029, doi:10.1053/j.gastro.2017.10.050.

19. de Araujo Junior, R.F.; Eich, C.; Jorquera, C.; Schomann, T.; Baldazzi, F.; Chan, A.B.; Cruz, L.J. Ceramide and palmitic acid inhibit macrophage-mediated epithelial-mesenchymal transition in colorectal cancer. Mol Cell Biochem 2020, 468, 153-168, doi:10.1007/s11010-020-03719-5.

20. He, Y.; Rezaei, S.; Júnior, R.F.d.A.; Cruz, L.J.; Eich, C. Multifunctional Role of Lipids in Modulating the Tumorigenic Properties of 4T1 Breast Cancer Cells.

International Journal of Molecular Sciences 2022, 23, 4240.

21. Lin, L.; Ding, Y.; Wang, Y.; Wang, Z.; Yin, X.; Yan, G.; Zhang, L.; Yang, P.; Shen, H. Functional lipidomics: Palmitic acid impairs hepatocellular carcinoma development by modulating membrane fluidity and glucose metabolism. Hepatology 2017, 66, 432-448, doi:10.1002/hep.29033.

22. Maly, I.V.; Hofmann, W.A. Effect of Palmitic Acid on Exosome-Mediated Secretion and Invasive Motility in Prostate Cancer Cells. Molecules 2020, 25, doi:10.3390/molecules25122722.

23. Md. Zafaryab1, Khalid Umar Fakhri1, Md. Asad Khan3, , Krishnan Hajela2, M. Moshahid A. Rizvi*1. *In vitro* Assessment of cytotoxic and apoptotic potential of Palmitic acid for Breast cancer Treatment. International Journal of Life Sciences Research 2019, 10.13140/RG.2.2.33419.13606, doi:10.13140/RG.2.2.33419.13606.

24. Zhu, S.; Jiao, W.; Xu, Y.; Hou, L.; Li, H.; Shao, J.; Zhang, X.; Wang, R.; Kong, D. Palmitic acid inhibits prostate cancer cell proliferation and metastasis by suppressing the PI3K/Akt pathway. Life Sci 2021, 286, 120046, doi:10.1016/j.lfs.2021.120046.

25. Feng, J.; Xiang, L.; Fang, C.; Tan, Y.; Li, Y.; Gong, T.; Wu, Q.; Gong, T.; Zhang, Z. Dual-Targeting of Tumor Cells and Tumor-Associated Macrophages by Palmitic Acid Modified Albumin Nanoparticles for Antitumor and Antimetastasis Therapy. ACS Appl Mater Interfaces 2022, 14, 14887-14902, doi:10.1021/acsami.1c23274.

26. Korbecki, J.; Bajdak-Rusinek, K. The effect of palmitic acid on inflammatory response in macrophages: an overview of molecular mechanisms. Inflamm Res 2019, 68, 915-932, doi:10.1007/s00011-019-01273-5.

27. Shen, K.Y.; Song, Y.C.; Chen, I.H.; Chong, P.; Liu, S.J. Depletion of tumor-associated macrophages enhances the anti-tumor immunity induced by a Toll-like receptor agonist-conjugated peptide. Hum Vaccin Immunother 2014, 10, 3241-3250, doi:10.4161/hv.29275.

28. Tsai, Y.W.; Lu, C.H.; Chang, R.C.; Hsu, Y.P.; Ho, L.T.; Shih, K.C. Palmitoleic acid ameliorates palmitic acid-induced proinflammation in J774A.1 macrophages via TLR4-dependent and TNF-alpha-independent signallings. Prostaglandins Leukot Essent Fatty Acids 2021, 169, 102270, doi:10.1016/j.plefa.2021.102270.

29. Chai, F.; Sun, L.; He, X.; Li, J.; Liu, Y.; Xiong, F.; Ge, L.; Webster, T.J.; Zheng, C. Doxorubicin-loaded poly (lactic-co-glycolic acid) nanoparticles coated with

chitosan/alginate by layer by layer technology for antitumor applications. Int J Nanomedicine 2017, 12, 1791-1802, doi:10.2147/IJN.S130404.

30. Choi, Y.; Yoon, H.Y.; Kim, J.; Yang, S.; Lee, J.; Choi, J.W.; Moon, Y.; Kim, J.; Lim, S.; Shim, M.K., *et al*. Doxorubicin-Loaded PLGA Nanoparticles for Cancer Therapy: Molecular Weight Effect of PLGA in Doxorubicin Release for Controlling Immunogenic Cell Death. Pharmaceutics 2020, 12, doi:10.3390/pharmaceutics12121165.

31. Da Silva, C.G.; Camps, M.G.M.; Li, T.M.W.Y.; Zerrillo, L.; Löwik, C.W.; Ossendorp, F.; Cruz, L.J. Effective chemoimmunotherapy by co-delivery of doxorubicin and immune adjuvants in biodegradable nanoparticles. Theranostics 2019, 9, 6485-6500, doi:10.7150/thno.34429.

32. Wang, J.; Shi, A.; Agyei, D.; Wang, Q. Formulation of water-in-oil-in-water (W/O/W) emulsions containing trans-resveratrol. RSC Advances 2017, 7, 35917-35927, doi:10.1039/c7ra05945k.

33. Ortega-Oller, I.; Padial-Molina, M.; Galindo-Moreno, P.; O'Valle, F.; Jodar-Reyes, A.B.; Peula-Garcia, J.M. Bone Regeneration from PLGA Micro-Nanoparticles. Biomed Res Int 2015, 2015, 415289, doi:10.1155/2015/415289.

34. Chittasupho, C.; Lirdprapamongkol, K.; Kewsuwan, P.; Sarisuta, N. Targeted delivery of doxorubicin to A549 lung cancer cells by CXCR4 antagonist conjugated PLGA nanoparticles. Eur J Pharm Biopharm 2014, 88, 529-538, doi:10.1016/j.ejpb.2014.06.020.

35. Doddagoudar, S.R.; Sreenivas, A.G.; Ramappa, K.T.; Nidoni, U.; Hiregoudar, S.; Yerragopu, P.S. Chemical Synthesis of Silver Nanoparticles Using Tri-sodium Citrate, Stability Study and Their Characterization. International Research Journal of Pure and Applied Chemistry 2020, 10.9734/irjpac/2020/v21i330159, 37-50, doi:10.9734/irjpac/2020/v21i330159.

36. Percie du Sert, N.; Hurst, V.; Ahluwalia, A.; Alam, S.; Avey, M.T.; Baker, M.; Browne, W.J.; Clark, A.; Cuthill, I.C.; Dirnagl, U., *et al*. The ARRIVE guidelines 2.0: Updated guidelines for reporting animal research. PLOS Biology 2020, 18, e3000410, doi:10.1371/journal.pbio.3000410.

37. Charafe-Jauffret, E.; Tarpin, C.; Bardou, V.J.; Bertucci, F.; Ginestier, C.; Braud, A.C.; Puig, B.; Geneix, J.; Hassoun, J.; Birnbaum, D., *et al*. Immunophenotypic analysis of inflammatory breast cancers: identification of an 'inflammatory signature'. J Pathol 2004, 202, 265-273, doi:10.1002/path.1515.

38. Rôxo, V.B.d.S.; Moron, S.E.; Ferreira, D.A.; Jorge, M.P.B. Crude glycerol in the diets of the juveniles ofAmazon catfish (female Pseudoplatystoma

punctifer × male Leiarius marmoratus). International Journal of Environment, Agriculture and Biotechnology 2018, 3, 1640-1655, doi:10.22161/ijeab/3.5.10.

39. Peixoto, R.C.; Miranda-Vilela, A.L.; de Souza Filho, J.; Carneiro, M.L.; Oliveira, R.G.; da Silva, M.O.; de Souza, A.R.; Bao, S.N. Antitumor effect of free rhodium (II) citrate and rhodium (II) citrate-loaded maghemite nanoparticles on mice bearing breast cancer: a systemic toxicity assay. Tumour Biol 2015, 36, 3325-3336, doi:10.1007/s13277-014-2966-x.

40. Bertrand, N.; Wu, J.; Xu, X.; Kamaly, N.; Farokhzad, O.C. Cancer nanotechnology: the impact of passive and active targeting in the era of modern cancer biology. Adv Drug Deliv Rev 2014, 66, 2-25, doi:10.1016/j.addr.2013.11.009.

41. Jayasingam, S.D.; Citartan, M.; Thang, T.H.; Mat Zin, A.A.; Ang, K.C.; Ch'ng, E.S. Evaluating the Polarization of Tumor-Associated Macrophages Into M1 and M2 Phenotypes in Human Cancer Tissue: Technicalities and Challenges in Routine Clinical Practice. Front Oncol 2019, 9, 1512, doi:10.3389/fonc.2019.01512.

42. Quan, H.; Kim, Y.; Wu, L.; Park, H.C.; Yang, H.C. Modulation of Macrophage Polarization by Phospholipids on the Surface of Titanium. Molecules 2020, 25, doi:10.3390/molecules25112700.

43. Schrors, B.; Boegel, S.; Albrecht, C.; Bukur, T.; Bukur, V.; Holtstrater, C.; Ritzel, C.; Manninen, K.; Tadmor, A.D.; Vormehr, M., *et al*. Multi-Omics Characterization of the 4T1 Murine Mammary Gland Tumor Model. Front Oncol 2020, 10, 1195, doi:10.3389/fonc.2020.01195.

44. Richards, C.H.; Mohammed, Z.; Qayyum, T.; Horgan, P.G.; McMillan, D.C. The prognostic value of histological tumor necrosis in solid organ malignant disease: a systematic review. Future Oncol 2011, 7, 1223-1235, doi:10.2217/fon.11.99.

45. MELICHAR, B.; ŠTUDENTOVÁ, H.; KALÁBOVÁ, H.; VITÁSKOVÁ, D.; ČERMÁKOVÁ, P.; HORNYCHOVÁ, H.; RYŠKA, A. Predictive and Prognostic Significance of Tumor-infiltrating Lymphocytes in Patients with Breast Cancer Treated with Neoadjuvant Systemic Therapy. Anticancer Research 2014, 34, 1115-1125.

46. Ibrahim, M.; Abuwatfa, W.H.; Awad, N.S.; Sabouni, R.; Husseini, G.A. Encapsulation, Release, and Cytotoxicity of Doxorubicin Loaded in Liposomes, Micelles, and Metal-Organic Frameworks: A Review. Pharmaceutics 2022, 14, doi:10.3390/pharmaceutics14020254.

47. Tsai, L.H.; Yen, C.H.; Hsieh, H.Y.; Young, T.H. Doxorubicin Loaded PLGA Nanoparticle with Cationic/Anionic Polyelectrolyte Decoration: Characterization, and Its Therapeutic Potency. Polymers (Basel) 2021, 13, doi:10.3390/polym13050693.

48. Rawat, P.S.; Jaiswal, A.; Khurana, A.; Bhatti, J.S.; Navik, U. Doxorubicin-induced cardiotoxicity: An update on the molecular mechanism and novel therapeutic strategies for effective management. Biomed Pharmacother 2021, 139, 111708, doi:10.1016/j.biopha.2021.111708.

49. Tao, X.; Gou, J.; Zhang, Q.; Tan, X.; Ren, T.; Yao, Q.; Tian, B.; Kou, L.; Zhang, L.; Tang, X. Synergistic breast tumor cell killing achieved by intracellular co-delivery of doxorubicin and disulfiram via core-shell-corona nanoparticles. Biomater Sci 2018, 6, 1869-1881, doi:10.1039/c8bm00271a.

50. Shafei, A.; El-Bakly, W.; Sobhy, A.; Wagdy, O.; Reda, A.; Aboelenin, O.; Marzouk, A.; El Habak, K.; Mostafa, R.; Ali, M.A., *et al*. A review on the efficacy and toxicity of different doxorubicin nanoparticles for targeted therapy in metastatic breast cancer. Biomed Pharmacother 2017, 95, 1209-1218, doi:10.1016/j.biopha.2017.09.059.

51. Piñón-Segundo, E.; G Nava-Arzaluz, M.; Lechuga-Ballesteros, D. Pharmaceutical polymeric nanoparticles prepared by the double emulsion-solvent evaporation technique. Recent Patents on Drug Delivery & Formulation 2012, 6, 224-235.

52. Giri, T.K.; Choudhary, C.; Ajazuddin; Alexander, A.; Badwaik, H.; Tripathi, D.K. Prospects of pharmaceuticals and biopharmaceuticals loaded microparticles prepared by double emulsion technique for controlled delivery. Saudi Pharm J 2013, 21, 125-141, doi:10.1016/j.jsps.2012.05.009.

53. Zerrillo, L.; Que, I.; Vepris, O.; Morgado, L.N.; Chan, A.; Bierau, K.; Li, Y.; Galli, F.; Bos, E.; Censi, R., *et al*. pH-responsive poly (lactide-co-glycolide) nanoparticles containing near-infrared dye for visualization and hyaluronic acid for treatment of osteoarthritis. J Control Release 2019, 309, 265-276, doi:10.1016/j.jconrel.2019.07.031.

54. Cruz, L.J.; van Dijk, T.; Vepris, O.; Li, T.; Schomann, T.; Baldazzi, F.; Kurita, R.; Nakamura, Y.; Grosveld, F.; Philipsen, S., *et al*. PLGA-Nanoparticles for Intracellular Delivery of the CRISPR-Complex to Elevate Fetal Globin Expression in Erythroid Cells. Biomaterials 2021, 268, 120580, doi:10.1016/j.biomaterials.2020.120580.

55. Lu, J.; Zhao, W.; Huang, Y.; Liu, H.; Marquez, R.; Gibbs, R.B.; Li, J.;

Venkataramanan, R.; Xu, L.; Li, S., *et al*. Targeted delivery of Doxorubicin by folic acid-decorated dual functional nanocarrier. Mol Pharm 2014, 11, 4164-4178, doi:10.1021/mp500389v.

56. Baumann, J.; Wong, J.; Sun, Y.; Conklin, D.S. Palmitate-induced ER stress increases trastuzumab sensitivity in HER2/neu-positive breast cancer cells. BMC Cancer 2016, 16, 551, doi:10.1186/s12885-016-2611-8.

57. Maceyka, M.; Spiegel, S. Sphingolipid metabolites in inflammatory disease. Nature 2014, 510, 58-67, doi:10.1038/nature13475.

58. Ryland, L.K.; Fox, T.E.; Liu, X.; Loughran, T.P.; Kester, M. Dysregulation of sphingolipid metabolism in cancer. Cancer Biol Ther 2011, 11, 138-149.

59. Yao, C.-H.; Fowle-Grider, R.; Mahieu, Nathanial G.; Liu, G.-Y.; Chen, Y., Jr.; Wang, R.; Singh, M.; Potter, Gregory S.; Gross, Richard W.; Schaefer, J., *et al*. Exogenous Fatty Acids Are the Preferred Source of Membrane Lipids in Proliferating Fibroblasts. Cell Chemical Biology 2016, 23, 483-493, doi:https://doi.org/10.1016/j.chembiol.2016.03.007.

60. Louie, S.M.; Roberts, L.S.; Mulvihill, M.M.; Luo, K.; Nomura, D.K. Cancer cells incorporate and remodel exogenous palmitate into structural and oncogenic signaling lipids. Biochim Biophys Acta 2013, 1831, 1566-1572, doi:10.1016/j.bbalip.2013.07.008.

61. Yu, G.; Luo, H.; Zhang, N.; Wang, Y.; Li, Y.; Huang, H.; Liu, Y.; Hu, Y.; Liu, H.; Zhang, J., *et al*. Loss of p53 Sensitizes Cells to Palmitic Acid-Induced Apoptosis by Reactive Oxygen Species Accumulation. Int J Mol Sci 2019, 20, doi:10.3390/ijms20246268.

62. Creemers, S.G.; van Koetsveld, P.M.; De Herder, W.W.; Dogan, F.; Franssen, G.J.H.; Feelders, R.A.; Hofland, L.J. *Mdr1* inhibition increases sensitivity to doxorubicin and etoposide in adrenocortical cancer. Endocr Relat Cancer 2019, 26, 367-378, doi:10.1530/ERC-18-0500.

63. Siddharth, S.; Nayak, A.; Nayak, D.; Bindhani, B.K.; Kundu, C.N. Chitosan-Dextran sulfate coated doxorubicin loaded PLGA-PVA-nanoparticles caused apoptosis in doxorubicin resistance breast cancer cells through induction of DNA damage. Sci Rep 2017, 7, 2143, doi:10.1038/s41598-017-02134-z.

64. Jin, X.; Mo, R.; Ding, Y.; Zheng, W.; Zhang, C. Paclitaxel-loaded N-octyl-O-sulfate chitosan micelles for superior cancer therapeutic efficacy and overcoming drug resistance. Molecular Pharmaceutics 2014, 11, 145-157.

65. Mu, L.M.; Ju, R.J.; Liu, R.; Bu, Y.Z.; Zhang, J.Y.; Li, X.Q.; Zeng, F.; Lu, W.L. Dual-functional drug liposomes in treatment of resistant cancers. Adv Drug

Deliv Rev 2017, 115, 46-56, doi:10.1016/j.addr.2017.04.006.

66. Akasov, R.; Drozdova, M.; Zaytseva-Zotova, D.; Leko, M.; Chelushkin, P.; Marc, A.; Chevalot, I.; Burov, S.; Klyachko, N.; Vandamme, T., *et al*. Novel Doxorubicin Derivatives: Synthesis and Cytotoxicity Study in 2D and 3D *in vitro* Models. Adv Pharm Bull 2017, 7, 593-601, doi:10.15171/apb.2017.071.

67. Rohan, T.E.; Arthur, R.; Wang, Y.; Weinmann, S.; Ginsberg, M.; Loi, S.; Salgado, R. Infiltrating immune cells in benign breast disease and risk of subsequent invasive breast cancer. Breast Cancer Res 2021, 23, 15, doi:10.1186/s13058-021-01395-x.

68. Zgura, A.; Galesa, L.; Bratila, E.; Anghel, R. Relationship between Tumor Infiltrating Lymphocytes and Progression in Breast Cancer. Maedica (Bucur) 2018, 13, 317-320, doi:10.26574/maedica.2018.13.4.317.

69. Lundgren, C.; Bendahl, P.O.; Ekholm, M.; Ferno, M.; Forsare, C.; Kruger, U.; Nordenskjold, B.; Stal, O.; Ryden, L. Tumour-infiltrating lymphocytes as a prognostic and tamoxifen predictive marker in premenopausal breast cancer: data from a randomised trial with long-term follow-up. Breast Cancer Res 2020, 22, 140, doi:10.1186/s13058-020-01364-w.

70. Hidalgo, M.A.; Carretta, M.D.; Burgos, R.A. Long Chain Fatty Acids as Modulators of Immune Cells Function: Contribution of FFA1 and FFA4 Receptors. Front Physiol 2021, 12, 668330, doi:10.3389/fphys.2021.668330.

71. Zhou, T.; Wang, G.; Lyu, Y.; Wang, L.; Zuo, S.; Zou, J.; Sun, L.; Zhao, W.; Shu, C.; Yang, Y.G., *et al*. Upregulation of SLAMF3 on human T cells is induced by palmitic acid through the STAT5-PI3K/Akt pathway and features the chronic inflammatory profiles of type 2 diabetes. Cell Death Dis 2019, 10, 559, doi:10.1038/s41419-019-1791-y.

72. Tinahones, F.; Gomez-Zumaquero, J.; Monzon, A.; Rojo-Martinez, G.; Pareja, A.; Morcillo, S.; Cardona, F.; Olveira, G.; Soriguer, F. Dietary palmitic acid influences LDL-mediated lymphocyte proliferation differently to other mono- and polyunsaturated fatty acids in rats. Diabetes Nutr Metab 2004, 17, 250-258.

73. De Palma, M.; Lewis, C.E. Macrophages limit chemotherapy. Nature 2011, 472, 303-304, doi:10.1038/472303a.

74. Hughes, R.; Qian, B.-Z.; Rowan, C.; Muthana, M.; Keklikoglou, I.; Olson, O.C.; Tazzyman, S.; Danson, S.; Addison, C.; Clemons, M., *et al*. Perivascular M2 Macrophages Stimulate Tumor Relapse after Chemotherapy. Cancer Research 2015, 75, 3479-3491, doi:10.1158/0008-5472.Can-14-3587.

75. Baghdadi, M.; Wada, H.; Nakanishi, S.; Abe, H.; Han, N.; Putra, W.E.; Endo, D.; Watari, H.; Sakuragi, N.; Hida, Y., *et al*. Chemotherapy-Induced IL34 Enhances Immunosuppression by Tumor-Associated Macrophages and Mediates Survival of Chemoresistant Lung Cancer Cells. Cancer Research 2016, 76, 6030-6042, doi:10.1158/0008-5472.Can-16-1170.

76. He, Y.; de Araujo Junior, R.F.; Cruz, L.J.; Eich, C. Functionalized Nanoparticles Targeting Tumor-Associated Macrophages as Cancer Therapy. Pharmaceutics 2021, 13, doi:10.3390/pharmaceutics13101670.

77. Larionova, I.; Cherdyntseva, N.; Liu, T.; Patysheva, M.; Rakina, M.; Kzhyshkowska, J. Interaction of tumor-associated macrophages and cancer chemotherapy. Oncoimmunology 2019, 8, 1596004, doi:10.1080/2162402x.2019.1596004.

78. Binker-Cosen, M.J.; Richards, D.; Oliver, B.; Gaisano, H.Y.; Binker, M.G.; Cosen-Binker, L.I. Palmitic acid increases invasiveness of pancreatic cancer cells AsPC-1 through TLR4/ROS/NF-kappaB/MMP-9 signaling pathway. Biochem Biophys Res Commun 2017, 484, 152-158, doi:10.1016/j.bbrc.2017.01.051.

79. Pan, J.; Fan, Z.; Wang, Z.; Dai, Q.; Xiang, Z.; Yuan, F.; Yan, M.; Zhu, Z.; Liu, B.; Li, C. CD36 mediates palmitate acid-induced metastasis of gastric cancer via AKT/GSK-3beta/beta-catenin pathway. J Exp Clin Cancer Res 2019, 38, 52, doi:10.1186/s13046-019-1049-7.

80. Pascual, G.; Dominguez, D.; Elosua-Bayes, M.; Beckedorff, F.; Laudanna, C.; Bigas, C.; Douillet, D.; Greco, C.; Symeonidi, A.; Hernandez, I., *et al*. Dietary palmitic acid promotes a prometastatic memory via Schwann cells. Nature 2021, 599, 485-490, doi:10.1038/s41586-021-04075-0.

81. Pereira, D.M.; Correia-da-Silva, G.; Valentao, P.; Teixeira, N.; Andrade, P.B. Palmitic acid and ergosta-7,22-dien-3-ol contribute to the apoptotic effect and cell cycle arrest of an extract from Marthasterias glacialis L. in neuroblastoma cells. Mar Drugs 2013, 12, 54-68, doi:10.3390/md12010054.

82. Rizzo, A.M.; Colombo, I.; Montorfano, G.; Zava, S.; Corsetto, P.A. Exogenous Fatty Acids Modulate ER Lipid Composition and Metabolism in Breast Cancer Cells. Cells 2021, 10, doi:10.3390/cells10010175.

83. Angerer, T.B.; Magnusson, Y.; Landberg, G.; Fletcher, J.S. Lipid Heterogeneity Resulting from Fatty Acid Processing in the Human Breast Cancer Microenvironment Identified by GCIB-ToF-SIMS Imaging. Analytical Chemistry 2016, 88, 11946-11954, doi:10.1021/acs.analchem.6b03884.

84. Eiriksson, F.F.; Nøhr, M.K.; Costa, M.; Bödvarsdottir, S.K.; Ögmundsdottir, H.M.; Thorsteinsdottir, M. Lipidomic study of cell lines reveals differences between breast cancer subtypes. PLoS One 2020, 15, e0231289, doi:10.1371/journal.pone.0231289.